Unravelling Photoinduced Electron Transfer Dynamics in Covalently Linked Bimetallic Complexes

Xiaolin Liu

A dissertation
submitted in partial fulfillment of the
requirements for the degree of

Doctor of Philosophy

University of Washington

2024

Reading Committee:
Xiaosong Li, Chair
Stefan Stoll
Cody W. Schlenker

Program Authorized to Offer Degree:
Chemistry

University of Washington

Abstract

Unravelling Photoinduced Electron Transfer Dynamics in Covalently Linked Bimetallic Complexes

Xiaolin Liu

Chair of the Supervisory Committee:
Xiaosong Li
Department of Chemistry

Photoinduced electron transfer (PET) processes are crucial in solar energy conversion and photocatalysis. Understanding the mechanism is very important to improve the efficiency and selectivity of PET. Bimetallic complexes that couple transition metal chromophores and catalytic centers with a bridging ligand are ideal molecular architectures for studying PET processes because they resemble photosynthetic molecules with multiple transition metal centers occurring in nature and through careful ligand design, explicit control of molecular geometry can be achieved. In this thesis, modern computational chemistry methods are employed to unravel excited state electronic and structural dynamics of bimetallic complexes. In Chapter 1, an introduction to the theoretical background in density functional theory and electron-nuclear dynamics is given. We then briefly review previous studies on bimetallic complexes and discuss the conformational differences in selected bimetallic complexes between the solution phase and solid state at ground state in Chapter 2. In Chapter 3, we study bridge-mediated metal-to-metal electron and hole transfer initiated by a photoinduced metal-to-ligand charge transfer excitation. In the last chapter, we establish the site-specificness of static nitrogen K-edge in the bimetallic complexes, laying the foundation for future time-resolved nitrogen K-edge experiments. Overall, the results shown in the thesis can help support static and time-resolved N K-edge X-ray absorption spectra experiments

on bimetallic complexes and provide insights into the rational design of these complexes.

TABLE OF CONTENTS

LIST OF FIGURES

ACKNOWLEDGMENTS

First of all, I would like to thank my advisor Professor Xiaosong Li for his guidance and support over the last five years. He taught me how to become a scientist through candid discussions, criticism, and patience. I would also like to thank my former and current committee members, Stefan Stoll, Cody W. Schlenker, Gerald T. Seidler, Munira Khalil, and David J. Masiello for their honest advice on improving my research.

Secondly, I am grateful to current and former members of the Li group. I would like to thank senior members Andrew Valentine, Tianyuan Zhang, and Xinzheng Yang for their mentoring and help. I would also like to thank Ryan Beck, Chad Hoyer, Linghua Zhu, Tian Wang, Diandong Tang, Hang Hu, Lixin Lu, Aodong Liu, Can Liao, and Maxwell Taub for their advice and helpful discussions.

Finally, I want to thank my experimental collaborators, Lin X. Chen, Amy Cordones-Hahn, Karen L. Mulfort, Zhu-Lin Xie, Elizabeth S. Ryland, Brian T. Phelan, and Pyosang Kim. As the Nobel laureate Professor Samuel C.C. Ting said, "An experiment can destroy the theory. A theory can never destroy an experiment. It's only when an experiment confronts a theory, you produce a new theory. And this is how science advances." I am lucky to collaborate with them and learn from them about photochemistry.

DEDICATION

to my parents

Chapter 1
INTRODUCTION

This chapter provides the theoretical foundation for the thesis. Density functional theory and its linear response time-dependent variant are used to obtain ground and excited state properties throughout the thesis and are introduced in the first part of the chapter. The second part introduces the Ehrenfest method, a mean-field approach to simulate non-adiabatic dynamics, which is employed in Chapter 3.

1.1 Density Functional Theory

1.1.1 Hohenberg–Kohn Theorems

In 1927, Llewellyn Thomas and Enrico Fermi proposed the Thomas-Fermi model[6,7] that treats electrons as a uniform electron gas, but the model is inaccurate and unpractical for chemical problems. In 1964, Walter Kohn and Pierre Hohenberg proved two theorems, which set the foundation for modern density functional theory(DFT).[8–10]

We consider N non-relativistic interacting electrons under external potential $v(\mathbf{r})$. The Hamiltonian can be written as:

$$H = T + V + U \tag{1.1}$$

$$= -\sum_i \frac{1}{2}\nabla_i^2 - \sum_i v(\mathbf{r}_i) + \sum_{i<j} \frac{1}{|\mathbf{r}_i - \mathbf{r}_j|} \tag{1.2}$$

The time-independent Schrödinger equation reads:

$$H\Psi = E\Psi \tag{1.3}$$

where the many-body wavefunction Ψ is a function of $3N$ spatial variables. The electron density $\rho(\mathbf{r})$, when integrated over space, gives the total number of electrons.

$$\int \rho(\mathbf{r}) d\mathbf{r} = N \tag{1.4}$$

The first theorem establishes the relationship between the ground state electron density $\rho(\mathbf{r})$ with external potential $v(\mathbf{r})$.

Theorem 1 (Hohenberg–Kohn Theorem 1) $\rho(\mathbf{r})$ *determines the external potential (to within an additive constant).*

According to Theorem 1, $\rho(\mathbf{r})$ determines the Hamiltonian, thus the many-body wavefunction and ground state energy. The wavefunction and energy can be written as functionals of the electron density, for example:

$$E[\rho(\mathbf{r})] = \int \rho(\mathbf{r}) v(\mathbf{r}) d\mathbf{r} + F[\rho(\mathbf{r})] \tag{1.5}$$

and $F[\rho(\mathbf{r})]$ gains its functional dependence on $\rho(\mathbf{r})$ from the wavefunction:

$$F[\rho(\mathbf{r})] = \int \Psi^*[\rho(\mathbf{r})](T+U)\Psi[\rho(\mathbf{r})] d\mathbf{r} \tag{1.6}$$

The functional dependence of energy and wavefunction with regard to electron density leads to Theorem 2.

Theorem 2 (Hohenberg–Kohn theorem 2) *The ground state density minimizes the total energy.*

In other words,

$$E[\rho(\mathbf{r})] \geq E[\rho_0(\mathbf{r})] \equiv E_0 \tag{1.7}$$

where ρ_0 and E_0 are ground state density and energy, respectively. This means we can obtain the ground state density variationally, but no practical way was proposed in their original paper.

1.1.2 Kohn-Sham DFT

In 1965, Walter Kohn and Lu Jeu Sham invented the Kohn-Sham method to solve for ground state density via the self-consistent field method.[11] Kohn and Sham constructed a fictitious system of *non-interacting* electrons that has the same density as the real system of interest where electrons do interact. The energy functional can be written as:

$$E[\rho] = \int v(\mathbf{r})\rho(\mathbf{r})d\mathbf{r} + T_s[\rho] + E_H[\rho] + E_{\text{xc}}[\rho] \tag{1.8}$$

where $\rho(\mathbf{r}) = \sum_i^N |\phi_i(\mathbf{r})|^2$ is electron density represented in one-electron wave functions.

$$T_s[\rho] = \sum_{i=1}^{N} -\frac{1}{2}\int \phi_i^*(\mathbf{r})\nabla^2\phi_i(\mathbf{r})d\mathbf{r} \tag{1.9}$$

is the kinetic energy,

$$E_H = \frac{1}{2}\int \frac{\rho(\mathbf{r})\rho(\mathbf{r}')}{|\mathbf{r}-\mathbf{r}'|}d\mathbf{r}d\mathbf{r}' \tag{1.10}$$

is the classical electron repulsion term, and $E_{\text{xc}}[\rho]$ is the exchange-correlation energy. In $E[\rho]$, the first three terms are usually very large, and $E_{\text{xc}}[\rho]$ is on the order of chemical interest.

To minimize the energy functional, we use the Euler-Lagrange method and arrive at a set of self-consistent Kohn-Sham equations:

$$h_i\phi_i = \epsilon_i\phi_i \tag{1.11}$$

where h_i is Kohn-Sham one-electron operator:

$$h_i = -\frac{1}{2}\nabla^2 + v(\mathbf{r}) + \int \frac{\rho(\mathbf{r}')}{|\mathbf{r}_i-\mathbf{r}'|}d\mathbf{r}' + v_{xc} \tag{1.12}$$

and

$$v_{xc}(\mathbf{r}) = \frac{\delta E_{\text{xc}}[\rho]}{\delta\rho(\mathbf{r})} \tag{1.13}$$

is the exchange-correlation potential. ϕ_i and ϵ_i are Lagrange multipliers and one-electron wavefunctions, respectively. Despite bearing no strict physical meaning, they have great semi-quantitive value in chemistry, interpreted as orbitals and orbital energies. According to Hohenberg–Kohn theorem, if the universal $E_{\mathrm{xc}}[\rho]$ is known, the accurate ground electronic state can be found by solving the Kohn-Sham equation self-consistently.

1.1.3 Exchange-correlation functionals

Because the exact form of E_{xc} is unknown, approximations must be made. Usually, we write it as:

$$E_{xc}[\rho] = \int \rho(\mathbf{r})\epsilon_{xc}[\rho(\mathbf{r})]d\mathbf{r} \tag{1.14}$$

$\epsilon_{xc}[\rho(\mathbf{r})]$ is exchange-correlation energy density. When local density approximation(LDA) is employed, it is functional of $\rho(\mathbf{r})$. LDA is a good approximation for slow-varying densities. The next level of treatment is called general gradient approximation(GGA), where the energy density is a functional of both $\rho(\mathbf{r})$ and $\nabla\rho(\mathbf{r})$.

Hybrid GGAs, where some exact Hartree-Fock exchange is incorporated, are the most popular functionals nowadays. For example, the famous B3LYP[12–15] functional is a hybrid GGA functional, which has the form:

$$E_{xc}^{B3LYP} = (1 - a_0 - a_x)\, E_x^{LSDA} + a_0 E_x^{HF} + a_x E_x^{B88} + (1 - a_c)\, E_c^{VWN} + a_c E_c^{LYP} \tag{1.15}$$

For B3LYP $a_0 = 0.20, a_x = 0.72, a_c = 0.81$. Some modern density functionals often include corrections for specific applications. To treat weak interactions well, one usually needs to include dispersion corrections, and to accurately describe charge-separated state, one needs to include long-range corrections. For example, the ωB97X-D functional[16] includes both corrections and will be employed in the thesis.

1.1.4 Time-dependent DFT

In 1984, Erich Runge and E. K. U. Gross extended the Hohenberg-Kohn theorems to time-dependent systems.[17–19] They proved that there is a one-to-one mapping between the time-dependent density and external potential for a many-body system evolving from a fixed initial state, provided that the external potential is Taylor expandable at the beginning. Runge-Gross theorem set the foundation of modern time-dependent DFT (TDDFT). There are two commonly used approaches to TDDFT, which are linear response and real-time approaches. Under weak perturbations, such as photo-excitation, linear response TDDFT[18] can provide accurate excitation energies and absorption profiles. For the study of strong perturbations and electronic dynamics, real-time TDDFT is often employed.[20,21] The two approaches are used in Chapters 3 and 4.

1.2 Electron-nuclear Dynamics

Photo-excitation creates non-equilibrium conditions for electronic and nuclear degrees of freedom. Full quantum mechanical treatment of both degrees of freedom is still very challenging except for the smallest systems. Mixed quantum-classical dynamics[22] is often the method of choice for simulating photo-induced electronic and nuclear dynamics in medium-sized molecules, where the electronic degrees of freedom are treated quantum mechanically and the nuclear degrees of freedom are treated classically. In this section, we introduce the Ehrenfest method,[23] which is suitable for simulating dynamics where there are high density of excited states. The derivations here closely follows Ref. 23–25.

We start with the time-dependent Schrödinger equation:

$$i\hbar\frac{\partial\Psi(\mathbf{r},\mathbf{R},t)}{\partial t} = H\Psi(\mathbf{r},\mathbf{R},t), \tag{1.16}$$

where $\mathbf{r}$ is electronic coordinate and $\mathbf{R}$ is nuclear coordinate. The molecular Hamiltonian is:

$$H = -\sum_a \frac{\hbar^2}{2M_a}\nabla_a^2 - \sum_i \frac{\hbar^2}{2m_i}\nabla_i^2 + V(\mathbf{R},\mathbf{r}) \tag{1.17}$$

$$= T_n(\mathbf{R}) + H_{el}(\mathbf{R},\mathbf{r}), \tag{1.18}$$

where i, j are electron indices and a, b are nuclear indices, $V(\mathbf{R}, \mathbf{r})$ includes electron-nuclear attraction, and electron-electron and nuclear-nuclear repulsions, T_n is the nuclear kinetic energy operator, and all the other terms are included in the electronic Hamiltonian, H_{el}.

The total wavefunction is $\Psi(\mathbf{r}, \mathbf{R}, t)$. We invoke the Born-Oppenheimer approximation and for simplicity of derivation, add a phase factor:

$$\Psi(\mathbf{r}, \mathbf{R}, t) = \phi(\mathbf{r}, t)\chi(\mathbf{R}, t)e^{\frac{i}{\hbar}\int^t E_{\mathbf{r}}(t')dt'}. \tag{1.19}$$

$\phi(\mathbf{r}, t)$ and $\chi(\mathbf{R}, t)$ are electronic and nuclear wavefunctions, respectively, and

$$E_{\mathbf{r}}(t) = \langle\Psi| H_{el} |\Psi\rangle_{\mathbf{r},\mathbf{R}} \tag{1.20}$$

, in which the subscript indicates coordinates that are integrated over.

We can fix the internal phase of the two wavefunctions:

$$i\hbar \langle\chi \mid \frac{\partial\chi}{\partial t}\rangle_{\mathbf{R}} = E \tag{1.21}$$

$$i\hbar \langle\phi \mid \frac{\partial\phi}{\partial t}\rangle_{\mathbf{r}} = E_{\mathbf{r}} \tag{1.22}$$

Substituting Eq. (1.19) and Eq. (1.18) into Eq. (1.16), projecting from left with $\chi(\mathbf{R}, t)$ and $\phi(\mathbf{r}, t)$ and integrating over $\mathbf{R}$ and $\mathbf{r}$ respectively, we have:

$$i\hbar\frac{\partial |\phi\rangle}{\partial t} = -\sum_i \frac{\hbar^2}{2m_i}\nabla_i^2 |\phi\rangle + \langle\chi| V |\chi\rangle_{\mathbf{R}} |\phi\rangle \tag{1.23}$$

$$i\hbar\frac{\partial |\chi\rangle}{\partial t} = -\sum_a \frac{\hbar^2}{2M_a}\nabla_a^2 |\chi\rangle + \langle\phi| H_{el} |\phi\rangle_{\mathbf{r}} |\chi\rangle \tag{1.24}$$

We can see that electronic degrees of freedom move in the average field of nuclear degrees of freedom, and vice versa. To treat nuclear degrees of freedom classically, we separate the nuclear wavefunction into real amplitude and phase factor:

$$\chi(\mathbf{R}, t) = A(\mathbf{R}, t)e^{\frac{i}{\hbar}S(\mathbf{R},t)} \tag{1.25}$$

Substituting it into Eq. (1.24) and separating out the real part:

$$\frac{\partial S}{\partial t} + \sum_a \frac{1}{2M_a} \left(\nabla_a S\right)^2 + \left\langle \phi \right| H_{el} \left| \phi \right\rangle_{\mathbf{r}} = i\hbar \sum_a \frac{1}{2M_a} \nabla_a^2 S \tag{1.26}$$

By taking the classical limit $\hbar \to 0$, we obtain the Hamilton-Jacobi equation:

$$\frac{\partial S}{\partial t} + \sum_a \frac{1}{2M_a} \left(\nabla_a S\right)^2 + \left\langle \phi \right| H_{el} \left| \phi \right\rangle_{\mathbf{r}} = 0 \tag{1.27}$$

This is equivalent to Newton's equation of motion, and we have:

$$F = -\nabla_{\mathbf{R}} \left\langle \phi \right| H_{el} \left| \phi \right\rangle_{\mathbf{r}} \tag{1.28}$$

In the classical limit, the nuclear wavefunction reduces to a delta function, Eq. (1.23) reduces to :

$$i\hbar \frac{\partial \left| \phi \right\rangle}{\partial t} = H_{el} \left| \phi \right\rangle \tag{1.29}$$

The last two equations define the Ehrenfest approach. We employ *ab initio* Ehrenfest method[26] in Chapter 3 to study photo-induced electron-nuclear dynamics.

Chapter 2

CONFORMATIONAL DIFFERENCES BETWEEN THE SOLUTION PHASE AND SOLID STATE IN SELECTED BIMETALLIC COMPLEXES

In order to study the structure-function relation and its implications on photo-induced electron transfer of bimetallic complexes, it is crucial that we have a good understanding of the molecular structures of these complexes in the solution phase since it is a common environment and excited state dynamics are highly responsive to solvent conditions. For solid-state, low-temperature single-crystal X-ray diffraction is a widely employed technique to reveal molecular structures. However, molecular structures in the solution phase are less straightforward. High-energy X-ray scattering and pair distribution function analysis(HEXS/PDF) is a powerful method to reveal the structure of materials lacking long-range order. Combined with density functional theory simulations, we demonstrate the application of HEXS/PDF with 0.26Å resolution to uncover the solution structure of five bimetallic Cu(I)/Ru(II)/Os(II) complexes. The metal-metal distance detected in solution is compared with that from the crystal structure and simulated models to confirm that distortions to the metal bridging ligand are unique to the solid state. This chapter is adapted with permission from Zhu-Lin Xie, Xiaolin Liu, Andrew J. S. Valentine, Vincent M. Lynch, David M. Tiede, Xiaosong Li, and Karen L. Mulfort, *Angew. Chem. Int. Ed.* ***2022****, 61, e202111764*.[5]

2.1 Introduction

Transition metal complexes (TMCs) have a rich diversity in structure arising from the versatility of coordination with ligands and donors from across the periodic table which enables their application in a broad range of areas such as catalysis, light harvesting, magnetism,

chemical absorption and separations.[27–31] As such, a key goal of research involving TMCs is to reveal the correlations that dictate how function follows molecular form. However, a complicating factor to accurately mapping activity in response to structure is that TMCs are typically used in a solution phase or complex environment that inhibits identification of molecular structure because of the lack of proper tools to directly probe the structure and particularly how it may change in a dynamic environment.

X-ray scattering characterization can fill in the gaps encountered with traditional methods of molecular structure confirmation (e.g. NMR, mass spectrometry, single-crystal X-ray diffraction). As a global, all-atom characterization technique, X-ray scattering can be used for pair distribution function (PDF) analysis, a Fourier transform of the oscillations observed in reciprocal space to yield pairwise atomic distances in real space.[32–35] By refining simulated structural models to the experimentally measured one-dimensional PDF patterns, one can directly visualize the molecular structure. As a result, X-ray scattering has been extensively applied to a wide variety of molecular materials including polymers,[36,37] metal oxides,[38–44] biomacromolecules,[45–48] aggregates of organic compounds[49–51] and supramolecular architectures.[52–60]

Advancements at synchrotron X-ray sources have enabled high-energy X-ray scattering (HEXS) capabilities, which drastically expands the q range up to ≈ 40 Å^{-1} and yields an achievable spatial resolution of ≈ 0.1Å.[61] This renders atomic resolution PDF analysis applicable to a wide range of samples[62–65] and has revealed detailed structure information comparable to solid-state X-ray diffraction. Petkov et al.[66] have demonstrated that HEXS/PDF can effectively uncover phase identity, relative abundance, and atomic structure from weakly scattering, low-Z disordered materials. Tiede et al. have used HEXS/PDF to determine the atomic level structure and domain size of thin films of an amorphous cobalt-based water oxidation catalyst material and link domain size with a choice of anion.[38,44] HEXS/PDF has also been applied to probe structure in more technically demanding solution environments. For example, the speciation of lanthanide/actinide ions in water has been revealed by HEXS/ PDF and has provided insights into the mechanisms of metal ion precipitation

from solution phase.[67–70] In battery materials, using HEXS/PDF complexation of metal ions with solvent molecules or counterions have been discovered to be responsible for the special electrochemical stability and ion conduction mechanism of electrolytes.[71,72] HEXS/PDF analysis has also uncovered solvent restructuring at the surface of nanoparticles which has important implications for materials function and has expanded the tunable parameter space for optimizing activity.[73,74] As these examples show, HEXS/PDF is an effective method for the structural determination of discrete molecules and clusters in the solid and solution state. However, HEXS/PDF analysis is yet not routinely applied to monitor structure of solution phase (supra)molecular complexes with a well-defined ligand motif. Most investigations in TMCs still heavily rely on low-temperature single-crystal X-ray diffraction as a proxy for solution structure when rationalizing properties.

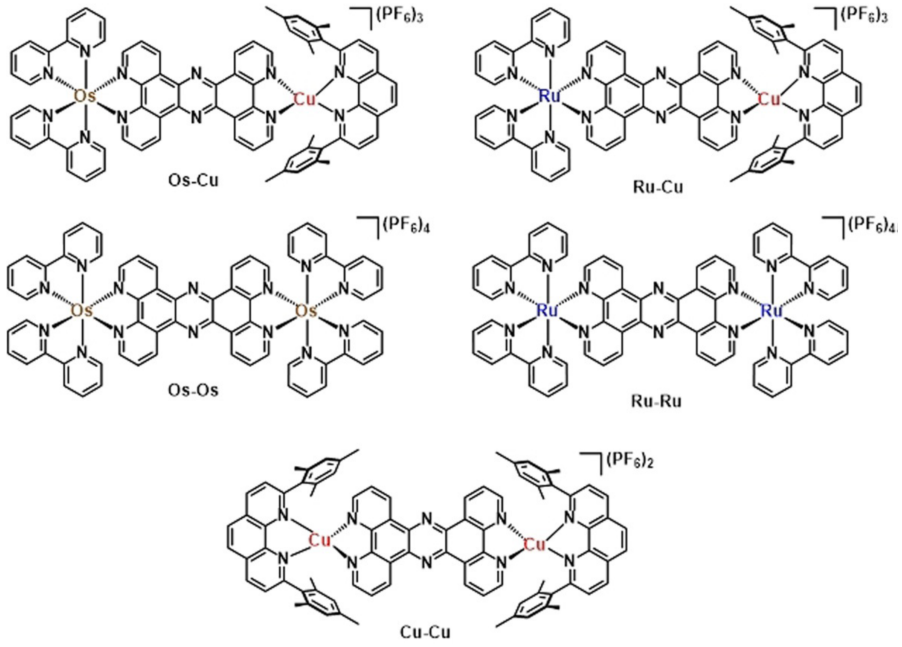

Figure 2.1: Chemical structures of the hetero- and homobimetallic complexes studied in this work. All five complexes are bridged by the conjugated tetrapyrido[3,2-a:2′,3′-c:3″,2′-h:2‴,3‴-j]phenazine (tpphz) ligand. Photoactive Cu, Ru or Os metal centers are installed on both sides of the tpphz ligand.

In this work, we have used HEXS/PDF with 0.26Å spatial resolution to investigate the solution phase structure of five bimetallic complexes (Figure 2.1) consisting of Cu(I)/Ru(II)/Os(II) metal centers connected by the conjugated tetrapyrido[3,2-a:2′,3′-c:3″,2′-h:2‴,3‴-j]phenazine (tpphz) in acetonitrile. The solution phase PDFs for these five complexes confirm the local coordination environment of each metal center, distances in the second coordination sphere, and the long-range metal-metal distances across tpphz. Computational modeling has helped rationalize discrepancies in long-range distances between the solution and solid state by differences in the conformation of tpphz. This work provides a roadmap for how HEXS/PDF and computational analysis can be used to uncover solution structures of (supra)molecular complexes.

2.2 Results and Discussion

2.2.1 Characterization in Solution State

The synthesis details, ^{1}H NMR, IR, UV-vis and emission spectra, and cyclic voltammetry of the complexes in Figure 2.1 can be found in Ref 5 and the supporting information therein.

^{1}H NMR spectroscopy confirmed the identity and purity of each complex and was used to comment on changes to metal electronic structure or possible aggregation of the bimetallic complexes. Interestingly, the newly synthesized **Os-Cu** shows that the local chemical environment of the ground state of the Os(II) center is not impacted by that of Cu(I) center as evidenced by negligible shifts in proton resonances between the monometallic and bimetallic complexes. We interpret this observation as electronically decoupled local coordination environments, despite their connection through the π-conjugated tpphz ligand. The monometallic $[Os(bpy)_2(tpphz)](PF_6)_2$ shows a concentration-dependence of some proton signals in ^{1}H NMR,[75] but such change in chemical shift was not observed in the NMR of any of the bimetallic complexes, indicating that supramolecular aggregates are not present in solutions of these bimetallic complexes.

The UV/Vis absorption spectra of **Os-Cu** were measured in acetonitrile and the relevant

data are compared with published data for the other homo- and bimetallic complexes. **Os-Cu** has two absorption features associated with metal-to-ligand charge transfer (MLCT) at a similar wavelength to that of **Os-Os** (**Os-Cu**: 431, 478 nm; **Os-Os**: 432, 475 nm) which are assigned to M(d)→tpphz(π^*) or M(d)→bpy(π^*) transitions. However, the intensity of the two MLCT bands of **Os-Cu** are 15% lower than those of **Os-Os**, which is expected as Cu(I) phenanthroline complexes generally display lower extinction coefficients than Os(II) bipyridine complexes. Like other Os(II) polypyridyl complexes, the absorbance of the MLCT band of **Os-Cu** and **Os-Os** extends to almost 750 nm, which is related to the reduced energy gap between the ground state and the MLCT excited state and the increased intensity of spin-forbidden MLCT transitions (singlet-triplet).[76,77]

The room temperature emission of ($[Os(bpy)_2(tpphz)](PF_6)_2$, **Os-Os**, and **Os-Cu**) was recorded in acetonitrile to compare with previously published results for **Ru-Ru**, **Ru-Cu**, and **Cu-Cu**. $[Os(bpy)_2(tpphz)](PF_6)_2$ and **Os-Cu** are emissive at room temperature with λ_{em} at 735 and 730 nm, respectively, while **Os-Os** is non-emissive. The non-emissive nature of **Os-Os** has previously been attributed to the low excited state energy with respect to the ground state such that the lifetime of the MLCT state is too short and radiationless deactivation is dominant at room temperature.[77] Based on previous studies,[1,78–80] Cu(I) complexes with 2,9-H substitutions are non-emissive at room temperature and therefore the emission of **Os-Cu** most likely originates from the Os(II) center.

Cyclic voltammetry was performed on the Os(II) complexes in acetonitrile. The Cu(II/I) redox couple occurs at less oxidizing potentials than those of Ru(III/II) and Os(III/II). The E($Cu^{2+/1+}$) of **Os-Cu** appears at +0.54V vs. SCE, which is slightly lower than the E($Cu^{2+/1+}$) of **Ru-Cu** and **Cu-Cu** (+0.55 V and +0.58 V vs. SCE, respectively). In addition, all the Cu(II/I) redox processes are quasi-reversible as a result of the flattening distortion of the metal center in Cu(II) state.[81] The Os(III/II) redox potential for **Os-Cu** is +0.90V vs. SCE, comparable to that of **Os-Os** (+0.89V vs. SCE), and 0.43V more cathodic than the Ru(II/III) couple in Ru(II)tpphz complexes.[1,75]

2.2.2 HEXS/PDF Determination of Solution Structure

The solution phase structures of all five bimetallic complexes and three mononuclear reference complexes were interrogated by HEXS on 20 mM solutions in acetonitrile using 58.6 keV X-rays at Beamline 11-ID-B of the Advanced Photon Source (APS) at Argonne National Laboratory. Samples were charged in Kapton capillaries and the scattering signal was measured in transmission mode as shown in Figure 2.2. The high-energy X-ray source enabled us to measure the total scattering pattern in reciprocal space, I(q), with a range of 0.5 $Å^{-1} < q < 24$ $Å^{-1}$. The spatial resolution of the experiment is related to the maximal q value by the equation of $d = 2\pi/q_{max}$, thus this HEXS study achieved a spatial resolution of 0.26Å. PDFgetX2[82] was used to process the raw scattering data and generate the reduced scattering pattern S(q) and the real-space Fourier transform G(r) in real space.

The PDF patterns for heterobimetallic **Ru-Cu** and **Os-Cu** are compared with the sum of the G(r) of the relevant mononuclear complexes in Figure 2.2 B–D. All PDF patterns have several peaks between 1 Å$< r <$ 6 Å, and we can assign each one to a specific pairwise distance in the first and second coordination shells of the metal centers, as well as the P-F bond from the PF_6^- counterion. The close agreement between G(r) of the mononuclear model complexes and the bimetallic complexes in this region suggests that the tpphz bridging ligand and the distal metal center have little to no impact on local pairwise distances. We can also identify the scattering interaction between each metal center and the central pyrazine N atoms at approximately 6.3 Å. The intensity of each G(r) pattern quickly dampens with increasing r value but for each complex, there is a broad featureless hump between 6–10 Å which we assign to the solvation sphere surrounding the molecular complexes. The broadness of this feature suggests that the interactions between each complex and surrounding solvent molecules are fluxional and have little to no short-range order detectable by HEXS/PDF. Notably, in the G(r) of all the bimetallic complexes we observe a peak between 12–13 Å that is completely absent in the mononuclear model complexes. We assign this feature to long-range metal-to-metal distances across the tpphz bridging ligand. Importantly, the order

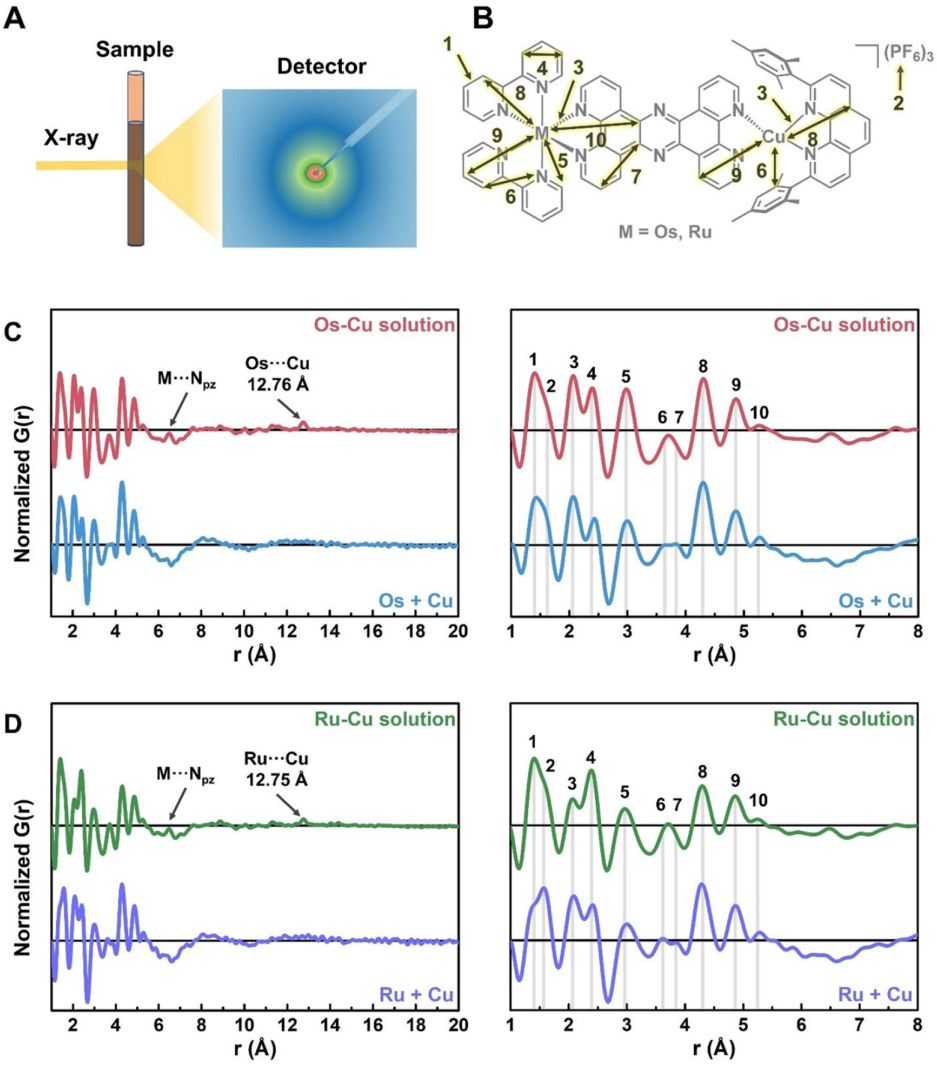

Figure 2.2: A) Experimental setup used in solution HEXS/PDF study showing raw detector image acquired at Beamline 11-ID-B of the Advanced Photon Source. B) Chemical structure of the heterobimetallic complexes in PDF analysis annotated with atomic pairwise distances. C, D) Comparison of the solution PDF patterns of **Os-Cu** and **Ru-Cu** to the sum of relevant monometallic modules. The peaks in the PDFs are assigned to corresponding pairwise distances in the chemical structure. **Os+Cu** stands for the sum of G(r) of $[Os(bpy)_2(Phen)](PF_6)_2$ and $[Cu(mesPhen)(Phen)](PF_6)$ and **Ru+Cu** for the sum of G(r) of $[Ru(bpy)_2(Phen)](PF_6)_2$ and $[Cu(mesPhen)(Phen)](PF_6)$. All samples were measured at 20 mM concentration in acetonitrile.

of M···M distance in solution follows with the order of atomic radius of the metal centers, that is, $d_{\mathbf{Cu\text{-}Cu}} < d_{\mathbf{Ru\text{-}Cu}} < d_{\mathbf{Os\text{-}Cu}} < d_{\mathbf{Ru\text{-}Ru}} < d_{\mathbf{Os\text{-}Os}}$. The observation and quantification of the M···M distance in solutions of the bimetallic complexes is a convenient handle by which to assess the impact of environmental perturbations on (supra)molecular conformation. The ^{1}H NMR and UV/Vis studies described above indicate that there is no strong intermolecular interactions observed with bimetallic complexes in solution phase. Previously, $[Os(bpy)_2\ (tpphz)]^{2+}$ was reported to show concentration-dependent NMR spectra due to the intermolecular $\pi - \pi$ stacking in solution[75,83] but none of the bimetallic complexes exhibit similar effects. We presume that as the steric hindrance on both sides of tpphz increases, the bimetallic complexes cannot approach too closely to adjacent molecules in solution to form strong intermolecular interactions.

2.2.3 Single-crystal X-ray Diffraction

Single crystal structures of **Cu-Cu**, **Os-Cu**, and **Os-Os** were obtained for the first time by low-temperature single-crystal X-ray Diffraction(XRD). These new structures are presented in Figure 2.3 and compared with previously described XRD structures of **Ru-Ru**[2] and **Ru-Cu**.[1] As expected, the crystal structures of **Os-Cu** and **Cu-Cu** reveal that the Cu(I) centers are heteroleptically coordinated by mesPhen and tpphz in a pseudotetrahedral geometry, in which the two bidentate ligands are not perpendicular to each other, but slightly flattened. We can quantify the deviation of the geometry from perfect tetrahedral by using the geometry index parameter s_4 which ranges from zero for perfect square planar to one for perfect tetrahedral.[84] The s_4 values for **Os-Cu**, **Ru-Cu** and **Cu-Cu** are 0.715, 0.720, and 0.656 respectively, indicating more deviation from tetrahedral is found in **Cu-Cu** than other two complexes. Like for previous CuHETPHEN crystal structures, intramolecular π-stacking between one of the mesityl groups of mesPhen with the phenanthroline moiety of tpphz yields the "pac-man" motif at the Cu(I) center.[85,86] Looking past the local coordination sphere of each metal center, a significant feature of the bridging tpphz ligand is its deviation from planarity in the solid state. We identify three types of deformation of the central ligand:

1) bowing, where the two ends of tpphz bend towards the same direction; 2) twisting, where the two ends of the ligand rotate in opposite directions along the axis containing two metal centers; and 3) waving, where the two ends of the ligand bend towards the opposite direction. The tpphz ligand of **Os-Cu** and **Ru-Cu**[1] both exhibit a bowing deformation (Figure 2.3), with the dihedral angle between the two phenanthroline moieties on tpphz calculated as 11.18° and 8.28°, respectively. The complex with a twisting deformation on tpphz is found in **Os-Os**, which gives rise to a dihedral angle of 8.28° between two phenanthroline moieties on tpphz. Despite being a structural congener of **Os-Os**, the central ligand of **Ru-Ru** shows a waving deformation in the crystal structure. Interestingly, in **Cu-Cu**, the tpphz ligand in the crystal structure exhibits only marginal structural variations from planarity.

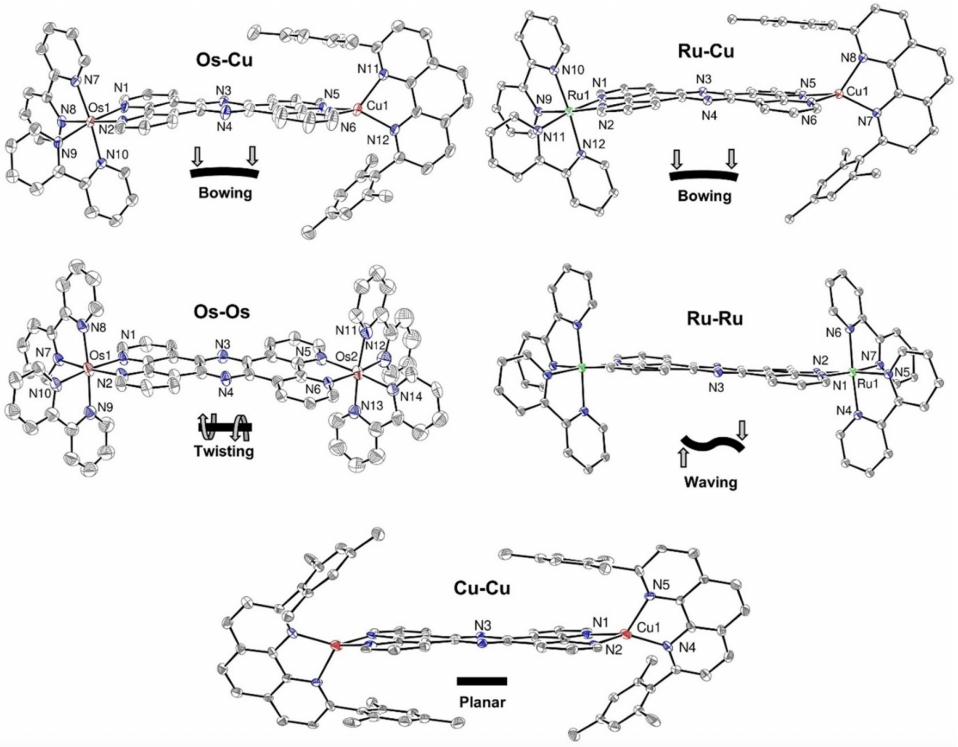

Figure 2.3: ORTEP diagrams for **Os-Cu**, **Os-Os**, **Ru-Cu**,[1] **Ru-Ru**[2] and **Cu-Cu** (30% thermal ellipsoids). H atoms and counterions (Cl^- for **Ru-Ru**, PF_6^- for others) are omitted for clarity.

Analysis of the full XRD structure reveals that various intermolecular forces are responsible for the deformation of tpphz in the bimetallic complexes. For example, in the crystal lattice of **Os-Cu** (Figure 2.4), the mesityl group (ring R1) interacts with the H atom on C36 of another complex, resulting in a C-H$\cdots\pi$ interaction with a distance of 3.087 Å. Similarly, the R2 ring on tpphz forms C-H$\cdots\pi$ interactions with C44 and C65 with a distance of 2.947 Å and 2.948 Å, respectively. In addition, $\pi - \pi$ interaction of the R3 ring of the mesPhens between adjacent molecules is observed in the crystal lattice. The short distances of these interactions enforce effective repulsions between the two metal centers and induce the bowing conformation of tpphz. The crystal packing patterns of **Ru-Cu** are analogous to those of **Os-Cu**, leading to similar structural distortion in the first coordination shells and the bridging ligand. The single-crystal structures of **Ru-Ru** and **Os-Os** also have significant intermolecular interactions which we hypothesize are responsible for the twisting and waving deformations observed in the tpphz ligand of these complexes. In contrast, there are no intermolecular interactions in the crystal packing of **Cu-Cu**, and tpphz in this complex is nearly perfectly planar. From this series of bimetallic complexes we venture that the severe deformations in tpphz are a direct result of intermolecular interactions, and in turn, substantially impact the intramolecular M$\cdots$M distances observed in the solid state. The M$\cdots$M distance of the complexes follows the order of $d_{\mathbf{Ru\text{-}Cu}} < d_{\mathbf{Os\text{-}Cu}} < d_{\mathbf{Cu\text{-}Cu}} < d_{\mathbf{Ru\text{-}Ru}} < d_{\mathbf{Os\text{-}Os}}$, in contrast with that found from PDF analysis.

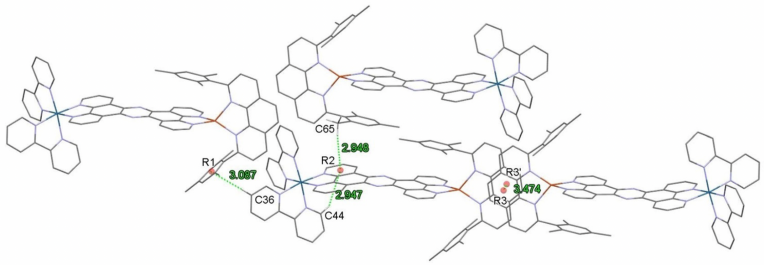

Figure 2.4: Interactions of **Os-Cu** complexes in crystal lattice that are responsible for the deformation of tpphz. H atoms and counterions (PF_6^-) are omitted for clarity. Numbers in green are distances of specific interactions in Å.

2.2.4 Computational Modelling

Energy-minimized DFT models of the bimetallic complexes were generated to help reconcile the differences observed between the M···M distances found from the solution PDF and single-crystal XRD structures of the bimetallic complexes, and a comparison of the energy-minimized DFT models with the crystal structures is presented in Figure 2.5.

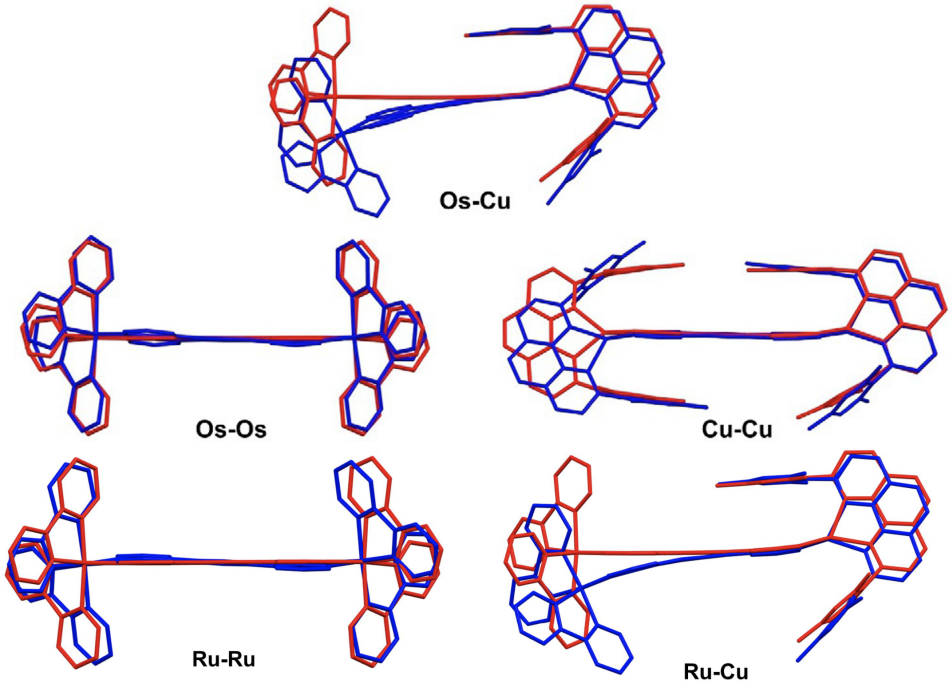

Figure 2.5: Overlay of the crystal structure (blue) and the DFT optimized structure (red) of **Os-Os**, **Os-Cu**, **Cu-Cu**, **Ru-Ru**, and **Ru-Cu**.

DFT calculations were performed using the ωB97X-D functional[16] with the LANL2DZ basis set[87] on transition metals and 6-31G(d) on light atoms. Solvent effects (acetonitrile) were considered using the polarizable continuum model (PCM)[88] to simulate the solvation environment in which the experimental HEXS/PDF study was performed. The hybrid ωB97X-D functional includes Grimme's D2 dispersion correction, which is important for simulation of non-covalent interactions.[16] The most striking difference between the DFT and

crystal structures is that all of the optimized, calculated structures of the bimetallic complexes present a flattened tpphz ligand, free of any of the distortions found by single-crystal XRD. **Os-Cu** displays the most noticeable difference between the crystal structure and the DFT model: the bend in the tpphz of the crystal structure leads to a change of 14.38° in the dihedral angle between the Os(II) module and the Cu(I) module as compared with the DFT model. In the case of the homobimetallic complexes where the tpphz deformations in the solid state are not as severe, the DFT models have a closer resemblance to the solid state but still do not capture the twisting and waving of tpphz found in **Ru-Ru** and **Os-Os**. To further assess whether the DFT calculations reflect a realistic solution structure, simulated scattering patterns were generated based on the optimized DFT models using SolX,[46] and PDF patterns in real space were obtained by Fourier transform of the simulated I(q). As compared to the experimentally acquired PDFs (Figure 2.6), we note that the simulated and experimental G(r)s are in excellent agreement in both short and mid-range distances, with two notable exceptions. First, the solution phase G(r) shows a peak at 1.45 Å which we assign to the P-F distance of PF_6^-. The PF_6^- counterions were not included in the DFT simulations since artificially fixing their position with respect to the complexes would lead to meaningless peaks in the simulated PDF. Second, the broad featureless solution sphere interactions seen in the experimental PDFs between 6–10 Å is also absent from the simulated PDF patterns. This is a reasonable discrepancy since the PCM models only reproduce the dielectric response of the solvent and not necessarily semi-ordered solvent surrounding the complexes. Despite these two exceptions, the similarity of the experimental and calculated PDF patterns in the short range ($r < 6$ Å) indicate that the local coordination spheres of the metal centers in the DFT model structures accurately represent the bonding and molecular geometry in the solution phase.

The M···M distance of the bimetallic complexes is longer in the simulated PDF patterns than those in the solution PDF and the distance measured in the crystal structure (Figure 2.7). However, the largest difference between the M···M distance observed in the simulated and solution PDFs is only 0.07 Å. This is a remarkably small error considering

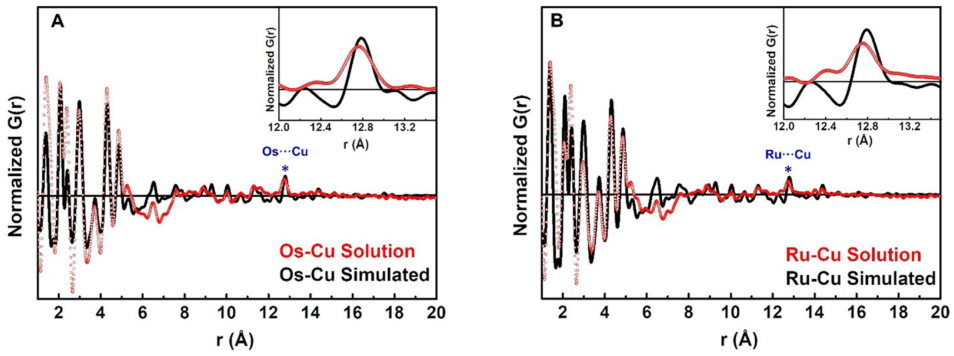

Figure 2.6: Solution (red dotted line) and calculated (black line) PDF patterns of A) **Os-Cu** and B) **Ru-Cu**. The inset shows the peak corresponding to the M···M distances.

that the M···M distance covers 10 bonds, translating to a sub 0.01 Å difference per bond as compared to the solution data. The trend in M···M distance found in the DFT models is $d_{\mathbf{Cu\text{-}Cu}} < d_{\mathbf{Ru\text{-}Cu}} \approx d_{\mathbf{Os\text{-}Cu}} < d_{\mathbf{Os\text{-}Os}} \approx d_{\mathbf{Ru\text{-}Ru}}$, which is the same as the experimental solution PDFs (Figure 2.7). This correlation between the DFT simulations and the solution phase HEXS/PDF measurements strongly suggests that the tpphz ligand of the bimetallic complexes maintains planarity in solution in a sterically relaxed mode.

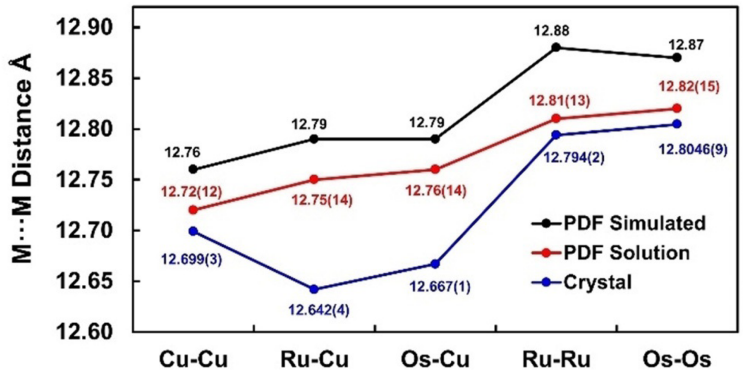

Figure 2.7: Comparison of the M···M distance of bimetallic complexes in the crystal structure, solution PDF, and simulated PDF. The uncertainties of the distances from the solution PDF are shown in parentheses and are estimated by the full-width-at-half-maximum (FWHM) of the peaks corresponding to the M···M distance in G(r).

2.2.5 Interpretation of Solution Phase PDF by Computational Models

We can use all of the experimental observations and computational models to describe the solution phase structure and conformation, primarily using the measured and calculated M···M distance as the key metric for comparison. When comparing the M···M distances among the three different structural datasets (solution PDF, solid-state crystal structure, DFT models) we note that the trend in M···M distance of the solution PDF matches that found in the DFT models (Figure 2.7). For the homobimetallic complexes **Cu-Cu**, **Ru-Ru**, and **Os-Os**, the M···M distances observed in the solution PDF agree slightly better with the values from their crystal structures than those of the DFT models (Figure 2.7) (Δ(M···M solution-solid)= 0.02–0.03 Å; Δ(M···M DFT-solution)=0.04–0.07 Å). However, as we can see in Figure 2.5, deviations of tpphz from planarity in the solid state of these complexes are quite minimal. From these small and comparable differences between the solid state/solution phase/DFT models it is difficult to distinguish the structure model (solid state or DFT) most closely represents the solution phase structure, since both have a relatively planar tpphz ligand.

For the heterobimetallic complexes **Ru-Cu** and **Os-Cu** which exhibit severe distortions to tpphz in the solid state, we observe a closer agreement between the solution PDF and the DFT models (Δ(M···M solution-solid)=0.10–0.11 Å; Δ(M···M DFT-solution)=0.03–0.04 Å). This indicates that the extreme bending of the tpphz ligand greatly shortens the M···M distance in solid state structure and the solution state structure should be free from such conformational distortions. Specific considerations for the distortion of tpphz in the solid state structures of **Ru-Cu** and **Os-Cu** are the conformational flexibility of the Cu(I) coordination and the close intermolecular interactions found between the $M(bpy)_2$ modules (where M=Ru(II) or Os(II); for example, see Figure 2.4). It is well documented that Cu(I)bis(phenanthroline) complexes routinely exhibit distortions from perfect tetrahedral geometry, and the severity of which is highly dependent on the 2,9-phenanthroline substitution.[85,86,89] Specifically to **Ru-Cu** and **Os-Cu**, CuHETPHEN model complexes typically

favor the "pac-man" orientation in which one mesityl group of mesPhen is stacked with the secondary phenanthroline ligand.[85,86]This has been noted in several crystal structures, but importantly this preferential π-stacking is not observed by other analytical techniques like NMR, and is presumed to be fast on the NMR timescale and therefore a fluxional interaction only resolved in the solid state. Additionally, the relatively small steric bulk of the 2,2′-bpy ligands on Ru(II) and Os(II) allows for close intermolecular $\pi - \pi$ interactions in the solid state. We presume that these factors together contribute to the large tpphz distortion in the solid state and therefore the significant difference we observe in the M···M distance measured by solution phase HEXS/PDF.

It is worth noting that this discussion about solution structure is based on models in thermodynamic equilibrium, but we also recognize the kinetic aspect of a molecule in solution and that these TMCs are in a constant state of motion. Indeed, the vibrational modes of the bimetallic complexes corresponding to distortion of tpphz features have vibrational frequencies at a magnitude of tens of wavenumber(Figure 2.8). This low value indicates that small perturbations, such as temperature change and solvent interactions, may also induce distortions in tpphz. The solution structure revealed by the HEXS/PDF measurements should be interpreted as an average of the total conformational landscape.

2.3 Conclusion

HEXS/PDF analysis was performed on five bimetallic TMCs with photoactive metal centers (Cu(I), Ru(II), and Os(II)) bridged by tpphz to quantitatively determine their solution phase structure and conformation. Spectroscopic analyses demonstrate that the TMCs do not form supramolecular aggregates in solution and that they are free from strong intermolecular interactions. HEXS/PDF analysis of each bimetallic TMC in acetonitrile solution confirmed all of the expected atomic pairwise distances in the first and second coordination shells of each metal center, and we have also observed long-range, over 12 Å, metal···metal distances across the tpphz bridging ligand. The M···M distance from the solution PDF pattern is a convenient experimental observable that we used to compare with solid-state single-crystal

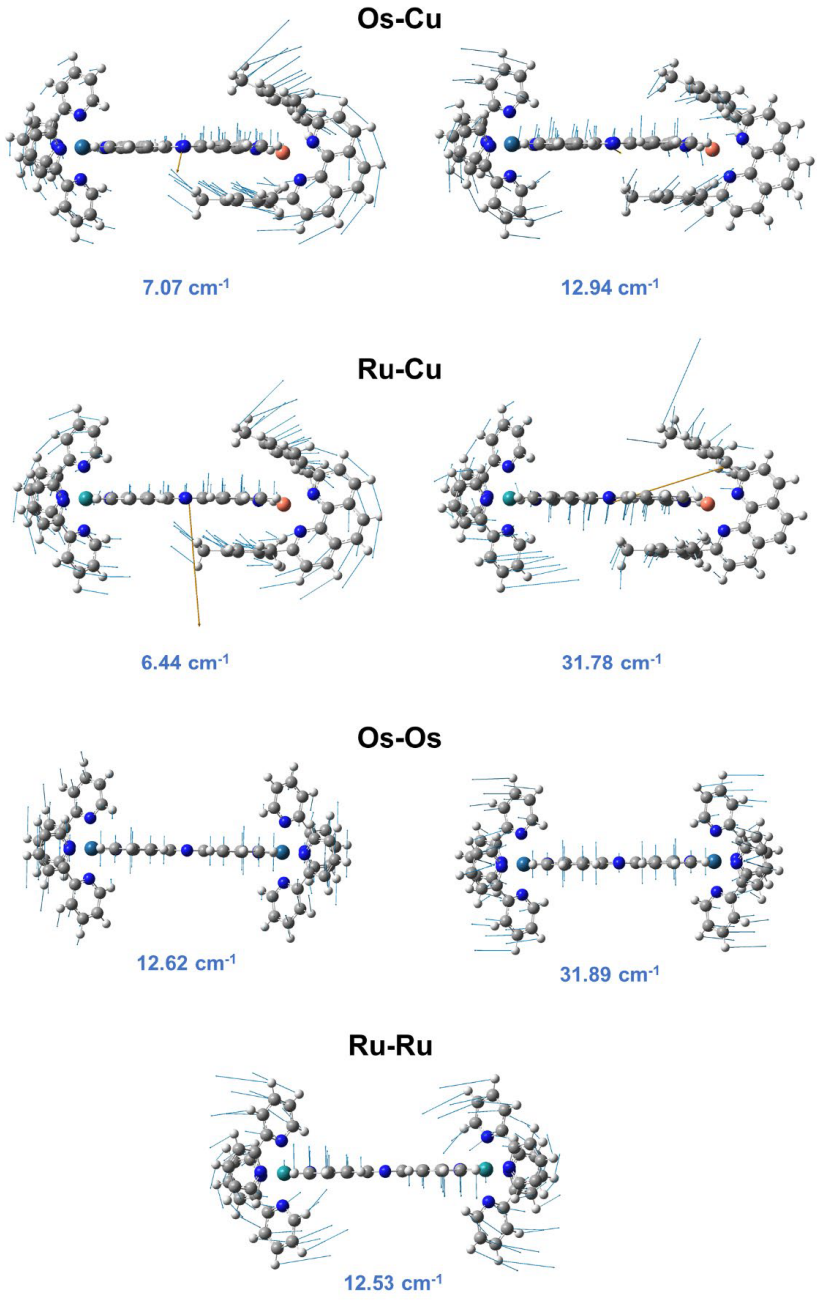

Figure 2.8: Calculated vibration modes and frequencies corresponding to the distortion of central ligand. Blue arrows are displacement vectors and orange arrows are dipole derivative unit vectors.

X-ray structures and DFT models of each bimetallic TMC. The M···M distance found in solution is greater than that found in the solid state, and careful examination of each single-crystal structure reveals intermolecular interactions between the ancillary ligands of the metal centers, which prompts the distortions in tpphz and the observed M···M distance. In striking contrast to the solid state structures, all DFT models feature a completely relaxed, planar tpphz ligand. The trend in M···M distance observed in solution by HEXS/PDF follows that found in the DFT models of each isolated bimetallic complex. This correlation, coupled with no spectroscopic evidence for aggregation or intermolecular interactions in solution, lead us to conclude that in solution, regardless of the metal centers, the bridging tpphz ligand occupies a planar geometry like that found in the DFT models.

To our knowledge, this solution structural study of the bimetallic TMCs is the first report in which HEXS/PDF analysis was used to capture a sub-Å distinction between solution and solid-state structures with resolution comparable to X-ray crystallography. This work demonstrates the unique ability of HEXS/PDF analysis and provides an additional critical tool to describe the structure-function relationship of molecularly defined materials dissolved in solution. As demonstrated here, low-temperature single-crystal XRD fails to accurately depict the solution phase structure of these supramolecular TMCs, which we anticipate will be a general observation as HEXS/PDF is applied more routinely to the interrogation of solution phase molecular structures. This work also sets the foundation for pump-probe studies[90,91] with high resolution in both time and space to visualize the solution structure of molecular samples following perturbation by stimuli such as temperature, applied voltage, and photoexcitation.

Chapter 3

BRIDGE-MEDIATED METAL-TO-METAL ELECTRON AND HOLE TRANSFER IN SUPERMOLECULAR DINUCLEAR COMPLEX

Bimetallic electron donor-acceptor complexes can facilitate electron and energy transfer with excellent structural control through synthetic design. In this chapter, we investigate the photochemical dynamics in a Ru-Cu bimetallic complex after photoexcitation of the Ru-centered charge transfer state. The physical underpinnings of the metal-to-metal directional charge transfer process are unraveled via analyses of the quantum electronic dynamics and electron-nuclear trajectories. The effects of molecular vibrations in the photoexcited state on the charge transfer processes are also analyzed. This chapter is adapted with permission from Xiaolin Liu, Dugan Hayes, Lin X. Chen, and Xiaosong Li. *J. Phys. Chem. A* ***2023****, 127, 1831–1838.*[92]

3.1 Introduction

Inspired by molecules in natural photosynthesis, much attention has focused on the rational design of molecular complexes with multiple transition metal centers. Bimetallic electron donor-acceptor complexes are the simplest among them and are ideal molecular architectures for incorporating building blocks of transition metal chromophores. Tetrapyrido[3,2-a:2′,3′-c:3″,2′-h:2‴,3‴-j]phenazine (tpphz, Figure 3.1) has been used as the bridging ligand in the design and synthesis of bimetallic complexes, since the extended π system can potentially facilitate electron and energy transfer between metal centers.[75,93] The excited state dynamics of polypyridyl dinuclear complexes with a tpphz bridging ligand have been extensively studied. Flamigni *et al.* studied a Ru(II)-Ru(II) dinuclear complex bridged by tpphz and

revealed that there is an excited state interconversion between two metal-to-ligand charge transfer (MLCT) states.[94] Chiorboli and coworkers investigated the photophysical properties and solvent-dependent excited state decay dynamics of homo- and heterodinuclear complexes with Ru and Os centers.[76,77] The ultrafast intramolecular electron transfer in a Ru(II)-Co(III) complex has been studied using transient optical and X-ray spectroscopies.[90,95,96]

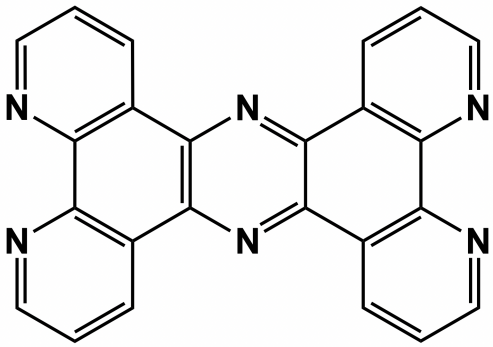

Figure 3.1: Structure of the tetrapyrido[3,2-a:2′,3′-c:3″,2′-h:2‴,3‴-j]phenazine (tpphz) ligand.

The synthetic strategy of CuHETPHEN (Cu(I) heteroleptic bis(1,10-phenanthroline)) has been used extensively in recent years because it provides exquisite structural control in the assembly of heteroleptic (and thus multi-functional) complexes with earth-abundant copper.[85,97–101] Combining the idea of using tpphz as a bridging ligand and the CuHETPHEN strategy, Hayes *et al.* synthesized a group of mononuclear and homo- and heterodinuclear complexes with Cu and/or Ru centers. Experimental studies using optical and X-ray transient absorption spectroscopy suggest that the bridging ligand in such bimetallic complexes plays an important role in the directional photoexcited charge transfer in addition to the redox properties of the metal centers.[1,100] This observation provides an important rational design principle for steering photochemical processes in bimetallic electron donor-acceptor complexes. Understanding the dynamics of photochemical processes and the interplay between ligands and metal centers is key to engineering high-efficiency solar cells and photocatalysts.[1,102–104] Theory and computation, especially modern time-dependent quantum

electronic dynamics, as complementary tools to spectroscopic probes, can provide atto- to femtosecond-resolved physical insights into the electronic and structural characteristics underlying experimental observations.[20,21]

In this work, we provide quantum mechanical insights into the ultrafast electronic and vibrational dynamics that underpin the directional photoexcited charge transfer in a bimetallic electron donor–bridge-acceptor complex. We seek to understand how the bridge and other metal-bound ligands modulate the excited state dynamics that results in the highly efficient directional charge transfer event.

3.2 Methodology

3.2.1 Real-Time Time-dependent Density Functional Theory and Ehrenfest Dynamics

In ultrafast photochemical dynamics, electronic degrees of freedom are in the non-equilibrium condition. Simulating such photochemical processes requires treatments of electronic coherence as well as non-equilibrium non-adiabatic energy transfer pathways.[20,21] The high density-of-excited-states nature of the molecular systems of interest makes Ehrenfest dynamics an ideal approach to simulate quantum dynamics within the time-dependent Schrödinger equation framework. In this work, we carried out *ab initio* on-the-fly Ehrenfest dynamics in the atomic orbital basis[26,105–109] to simulate the ultrafast electron-hole dynamics and their interplay with molecular vibrations.

As the *ab initio* Ehrenfest dynamics method has been previously developed and applied to modeling various ultrafast excited state electron-nuclear dynamics, we provide only a brief review of it here. We refer readers to recent reviews[20,21] for theoretical details. In *ab initio* Ehrenfest dynamics, the electronic degrees of freedom are explicitly propagated with real-time time-dependent density functional theory (RT-TDDFT). The electron-nuclear interactions responsible for the electronically non-adiabatic time evolution are modeled with the Ehrenfest technique, which propagates the nuclei on the time-evolving electronic potential.

The Ehrenfest dynamics scheme employed in this work takes advantage of an efficient triple-split operator integrator.[26] These different time steps reflect the characteristic timescales of the three different molecular equations-of-motion: nuclear motion driven by the velocity-Verlet algorithm with a time-step of Δt_N, the evolving time-dependent Kohn-Sham Hamiltonian with a time-step of Δt_{Ne}, and a unitary transformation RT-TDDFT used to propagate the electronic degrees of freedom with a time-step of Δt_e.

3.2.2 Initial Condition and Population Analysis

The photochemical dynamics start from the photoexcited MLCT state. A linear response TDDFT calculation suggests that the metal-to-ligand charge transfer transition involves several ligand orbitals. To facilitate the population analysis and prepare the initially photoexcited MLCT state, canonical orbitals are transformed to the natural transition orbitals (NTOs).[110,111] The total number of electrons is conserved in the process because the NTO transformation is unitary. In the NTO description, the MLCT excitation becomes a one-electron transition between orbitals. Therefore, the initial density at $t = 0$ fs is prepared by promoting one electron from the highest occupied to the lowest unoccupied NTO, resulting in a density matrix in the NTO basis. All occupied NTOs are used in constructing the one-electron density matrix and all NTOs are used in the population projection analysis. The NTO density matrix is transformed into the atomic orbital basis to initialize the quantum electron and electron-nuclear dynamics.

The on-the-fly population analysis is also carried out in the NTO basis. The time-dependent electron density matrix $\mathbf{P}(t)$ is projected to the ground state NTOs $\mathbf{C}_i$ computed at $t = 0$ and the occupation number of the i-th NTO is calculated as:

$$n_i(t) = \mathbf{C}_i(0)^\dagger \mathbf{P}(t) \mathbf{C}_i(0). \tag{3.1}$$

Note that population projection to the $t = 0$ ground state NTO space is valid only when the molecular geometry does not change in time.

3.3 Results and Discussion

All calculations were performed using a developmental version of the Gaussian software package.[112] The geometry of the bpy-Ru-tpphz-Cu-dmesp molecule (CuH_2-RuH_2 for short, Figure 3.2) molecule was optimized using the M06 functional[113] including Grimme's D3 dispersion.[114] The ultrafine grid option is used for the DFT numerical integration in the linear response TDDFT calculations. For quantum dynamics simulations, the fine grid option is employed. The LANL2DZ ECP basis[87] for Cu and Ru and SBJKC-VDZ basis[115,116] for light atoms were used in the geometry optimization. The Ehrenfest quantum dynamics calculations were performed using the same functional and basis sets. These basis sets were chosen because they reproduce important characteristics of the molecular geometry and UV-Vis spectrum calculated using a larger basis set but with a much lower computational cost for quantum dynamics. The step size of electronic dynamics is set to 0.0012 fs. The time steps in Ehrenfest dynamics are: $\Delta t_N = 0.15$ fs, $\Delta t_{Ne} = 0.015$ fs, and $\Delta t_e = 0.0015$ fs, according to the triple-split operator scheme.[26] Both dynamics were simulated for ∼200 fs.

3.3.1 Ground State Geometry and UV-Vis Spectrum

The optimized geometry of the CuH_2-RuH_2 bimetallic molecule is shown in Figure 3.2. The Ru atom bonds to two 2,2′-bipyridine (bpy) ligands and one side of the tpphz ligand. The Cu atom bonds to the 2,9-dimesityl-1,10-phenanthroline (dmesp) ligand and the other side of the tpphz ligand. To simplify notations, the molecule can be grouped into five parts: bpy-Ru-tpphz-Cu-dmesp. On the Cu-side of the structure, the two mesityl groups of the dmesp ligand are almost parallel to the tpphz ligand, suggesting strong $\pi-\pi$ interaction between ligand and bridge, similar to the "pac-man" motif in other Cu(I)-centered HETPHEN complexes.[1,5,117] The methyl substituents at 2,6-positions of the aryl groups prevent the dmesp ligand from rotating, resulting in a stable $\pi - \pi$ interaction. The bridging ligand remains in a flat configuration that provides an ideal pathway for electron transfer.

The UV-Vis spectrum of CuH_2-RuH_2 computed using linear response TDDFT is shown

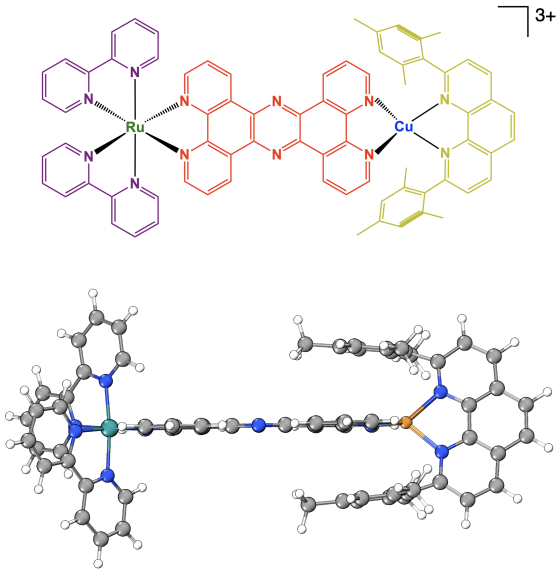

Figure 3.2: Structure of the bpy-Ru-tpphz-Cu-dmesp (CuH_2-RuH_2 for short) molecule. The 2,2′-bipyridine (bpy) ligands are shown in purple; the tetrapyrido[3,2-a:2′,3′-c:3″,2′-h:2‴,3‴-j]phenazine (tpphz) bridge is shown in red; and the 2,9-dimesityl-1,10-phenanthroline (dmesp) ligand is shown in yellow.

in Figure 3.3. The overall spectrum agrees with the experimental measurement,[1] where there is a broad feature in the 600-400 nm range (1.9∼3.1 eV). This low-energy band consists of MLCT transitions centered around the two metal sites. The lowest energy transitions all originate from the Cu center (see inset for a representative NTO transition pair for a selected Cu-centered MLCT excitation). While the excitations come from Cu $3d$ electrons, there is a dense manifold of accepting ligand orbitals delocalized throughout nearby ligands that give rise to the broad MLCT feature in the experimental spectrum. The Cu-center MLCT band continues to ∼480 nm (∼2.6 eV), where we start to see overlapping contributions from the Ru-centered MLCT excitations. The inset of Figure 3.3 shows the characteristics of a selected Ru-centered MLCT excitation which has similar characteristics to the Cu-centered band except with the electron excited from the Ru $4d$ orbitals.

In order to quantify the charge transfer characteristics, the molecular system is again

divided into five distinct groups as color-coded in Figure 3.2. Charge transfer matrix analysis[118,119] was carried out to quantify the amount of charge transfer between different molecular motifs. Particularly, this approach allows us to characterize the roles of different ligands (*e.g.*, tpphz, bpy, or dmesp) in the MLCT excitation. Charge transfer strengths are shown in Figure 3.3 for the selected MLCT transitions. In the Cu MLCT states, the charge moves mostly from Cu and nearby dmesp to the tpphz bridge ligand. For Ru-centered MLCT states, the charge transfer event occurs from Ru-*d* orbital to both the tpphz bridge and nearby bpy ligands. There is also significant inter-ligand charge transfer from the dmesp at the Cu site to the tpphz bridge ligand, similar to that observed for the Cu MLCT states. This observation highlights the long-range electronic coupling present in this system.

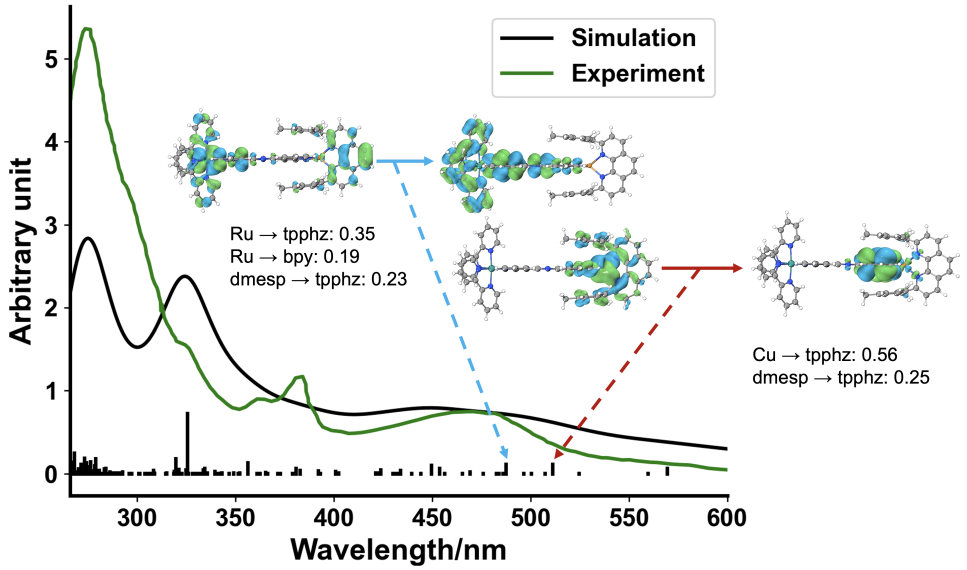

Figure 3.3: Absorption spectrum of $\mathbf{CuH_2\text{-}RuH_2}$ computed using linear response TDDFT. A Lorentzian broadening factor of 0.2 eV is used to plot the simulated spectrum. The experimental spectrum is digitized from Ref.[1] Natural transition orbitals of selected MLCT excitations are displayed with charge transfer matrix elements.

3.3.2 Quantum Electronic Dynamics

The spectral analysis above suggests that the tpphz bridging ligand plays an important role in the charge transfer events at the two metal centers. Cu- and Ru-centered MLCT states are coupled through the tpphz bridging ligand, which may provide an electron transfer pathway between the two metal centers. In this section, we carry out quantum electronic dynamics simulations to investigate the electron transfer pathways in the bpy-Ru-tpphz-Cu-dmesp bimetallic complex. With the electron-nuclear Ehrenfest dynamics, we also study the molecular structure change in the metal-to-metal charge transfer event.

The photochemical dynamics start from the Ru-center MLCT state prepared according to the procedure illustrated in the Methodology section. The Ru-center MLCT state is higher in energy than the Cu-center MLCT level, giving rise to an energetically feasible metal-to-metal charge transfer pathway. The photoexcited state arises from electronic transitions from Ru-d orbitals to the bpy ligands accompanied by charge transfer from dmesp ligand at the Cu site to the tpphz bridge (Figure 3.4A). After photoexcitation at $t = 0$ fs, the coherent electron-hole recombination takes place within 50 fs, shown in Figure 3.4A. While the photoexcited hole orbital repopulates to unity, the photoexcited electron does not deplete completely and still has a significant population at $t = 200$ fs. Detailed analysis suggests that the photoexcited hole receives additional electron populations from other occupied Ru-d orbitals, one of which is shown in Figure 3.4B. These selected orbital population evolutions shown in Figure 3.4 carry the important photophysics of interest. While there are some populations in other orbitals, they are considered as electronic structure reorganization in response to the photochemical processes.

The observation illustrated above from electronic dynamic simulations suggests that the photoexcited electron at the tpphz bridge can be persistent. This is because the photoexcited hole is filled quickly by electron transfer from other Ru-d electrons. These faster dynamics prevent a complete electron-hole recombination and therefore lead to a long-lived electron population at the tpphz bridge site and a significant population in the Ru-centered MLCT

state. Figure 3.5 plots the electron density difference snapshots as a function of time ($t = 0$, 50, and 200 fs) following excitation. It is clear to see there is a significant electron density residing at the tpphz bridge site even at 200 fs.

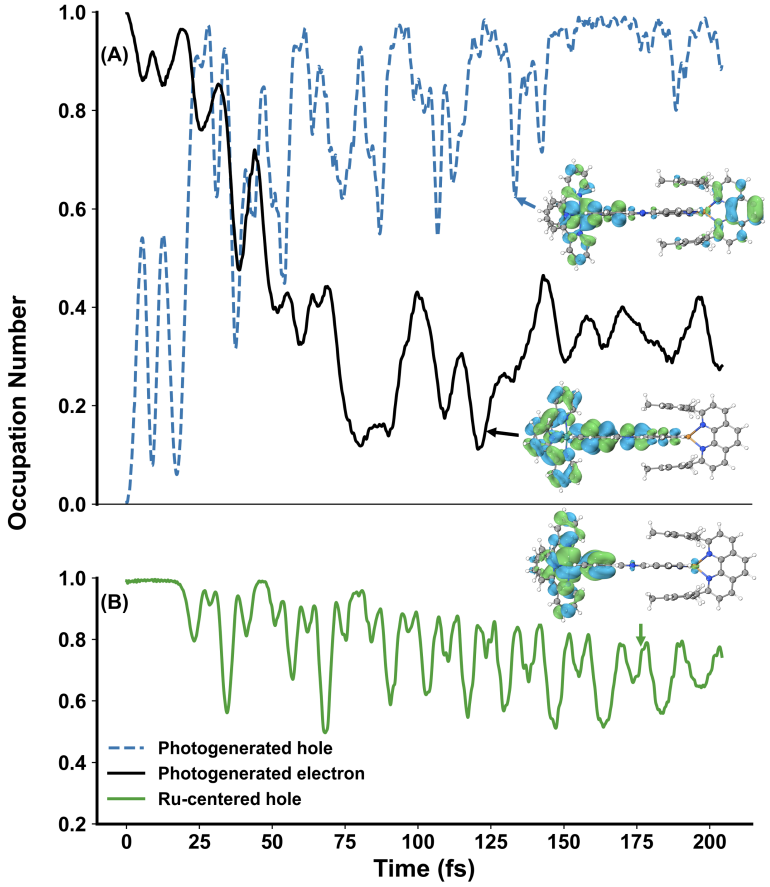

Figure 3.4: Time evolution of selected orbital populations after photoexcitation at $t = 0$ fs. Natural transition orbital (NTO) population analysis is carried out according to the procedure described in the Methodology section. NTOs are shown as insets. (**A**) Populations of the photoexcited electron (solid line) and hole (dashed line). (**B**) Population of a Ru-*d* orbital that transfers electron population to the photoexcited hole.

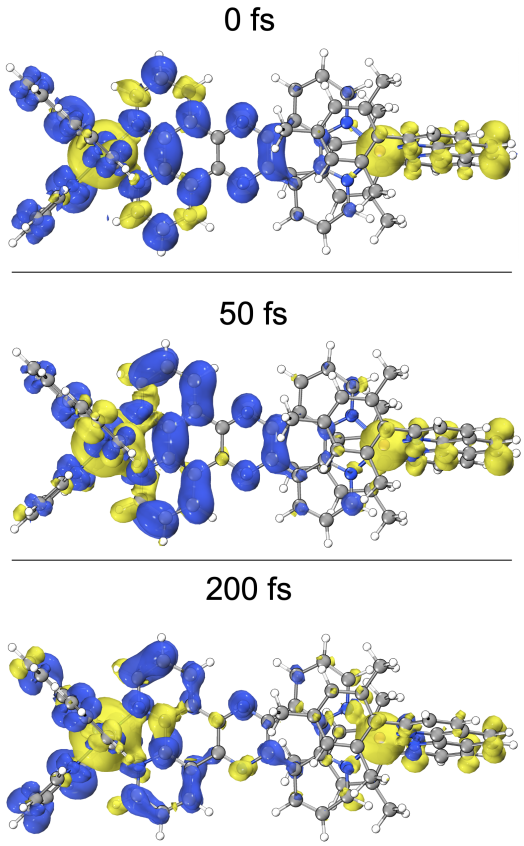

Figure 3.5: Electron density difference plots at $t = 0$, 50, and 200 fs. Electron density difference is computed as $\Delta\mathbf{P}(t) = \mathbf{P}(t) - \mathbf{P}_0(0)$ where $\mathbf{P}(t)$ is the time-dependent density matrix and $\mathbf{P}_0(0)$ is the ground state densitry matrix at $t = 0$ fs. An isovalue of 0.0004 is used. The blue/yellow color indicates an increased/decreased electron density compared to the ground state at $t = 0$ fs.

3.3.3 Electron-Nuclear Ehrenfest Dynamics

The dynamics discussed above describe the main electronic characteristics underlying the photoinduced charge transfer event in the bimetallic molecular complex. However, in the absence of nuclear dynamics, photochemical processes are reversible – a scenario that does not sustain directional metal-to-metal charge transfer. In order to understand the interplay between electronic and vibrational degrees of freedom during the charge transfer event and identify key molecular vibrations underlying the directional metal-to-metal charge trans-

fer, we carried out electron-nuclear Ehrenfest dynamics starting from the same Ru-centered MLCT state. The initial molecular structure is taken as the ground state minimum and will evolve according to the classical equation of motion on the RT-TDDFT potential energy surface.

Figure 3.6 shows the geometric changes compared to the initial ground state minimum. Noticeable changes are observed at 30 fs following the photoexcitation. For example, a small opening-closing motion of the mesityl ligands at the Cu site starts to occur. This vibrational motion changes the distance between the mesityl groups and the bridge by $\pm$0.003-0.005Å. In addition, a small out-of-plane vibration of the tpphz bridge ligand is observed with a $\sim$3.5° bending. At around 120 fs, which is the onset of the metal-to-metal electron transfer (MMET, see below) from Cu to Ru, a small rotation of the tpphz ligand along the Cu-Ru axis occurs, indicating a change of dominant vibrational mode. This mode is persistent until the end of our simulation. The rotation of the tpphz ligand can lead to a change of the dihedral angle between the tpphz and the backbone of the dmesp ligand, which is a key geometric feature of Cu(I) excitation. These small geometric changes identified in Figure 3.6 are possible vibrational driving forces underlying the directional metal-to-metal charge transfer event.

Figure 3.7 shows the time evolution of charge differences at the Ru, Cu, and tpphz bridge sites computed using the time-dependent densities from the electron-nuclear Ehrenfest dynamics. The charge difference is computed using time-dependent Mulliken population analysis with respect to the ground state at $t < 0$ fs. To better understand the charge transfer pathway, the charge evolutions of the Cu and Ru sides of the tpphz ligand are separately plotted.

Upon photoexcitation at $t = 0$ fs, both sides of the tpphz bridging ligand gain electron population from Ru-centered MLCT excitation. This analysis agrees with the charge transfer matrix elements shown in Figure 3.3. In the first $\sim$150 fs, two distinct oscillatory charge transfer events are observed, identified by their relative time-evolution phases: fast transfer between the Ru-sided tpphz and Cu-sided tpphz ligand, and slow transfer between Ru-d

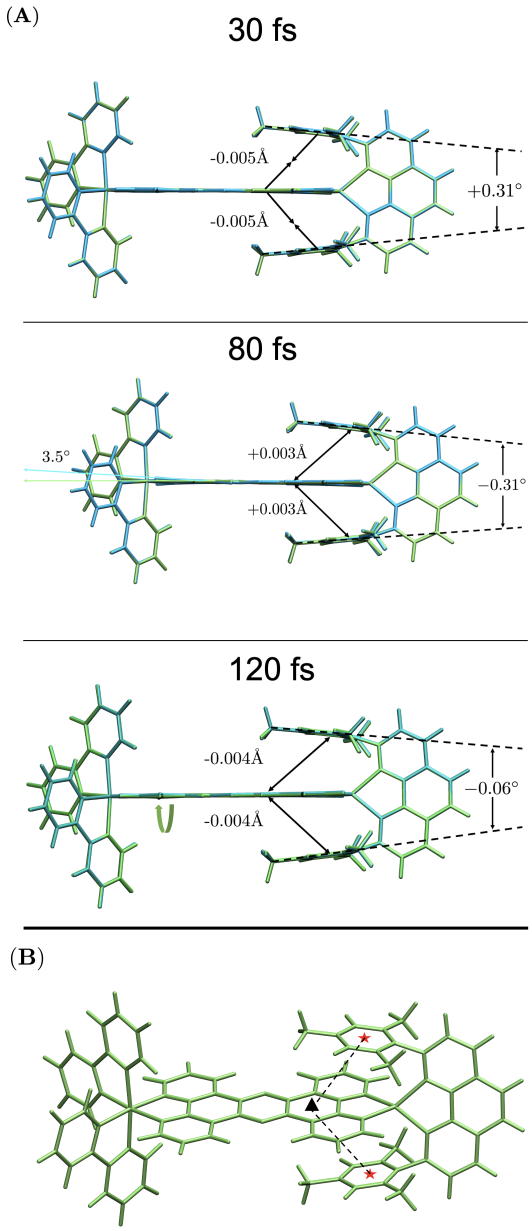

Figure 3.6: Geometric changes compared to the initial ground state structure. (**A**) Geometries at 30 fs, 80 fs, and 120 fs. The lime-colored molecule is the initial geometry and the cyan-colored are the geometry snapshots from the Ehrenfest dynamics. (**B**) The distance between the mesityl groups and the bridge is measured as the center of the benzene units of the mesityl group (red star) and the tpphz bridge (black triangle).

and Cu-*d* manifolds. The former is a clear signature of bridge-mediated electron transfer and the latter can be viewed as direct hole transfer between the metal centers. These two ultrafast charge transfer events are mostly correlated with the closing motion of the mesityl ligands at the Cu site and the rotational motion of the tpphz bridge (see Figure 3.6). Figure 3.9 shows the proposed mechanism underlying the observed photochemical process. After the photoexcitation to the Ru-centered MLCT state, there are concerted electron and hole transfer events taking place between the Ru-centered and Cu-centered MLCT states, giving rise to the characteristic metal-to-metal charge transfer process.

To confirm that these small geometric changes identified in Figure 3.6 are correlated with direction metal-to-metal charge transfer event, the Mulliken charge differences are Fourier transformed into the frequency domain and the possible vibrational modes that modulate the charge evolutions are shown in Figure 3.8. Fourier transform of the charge evolution shows that the dominant low frequencies are in the 600 to 900 cm^{-1} range. Analysis of the ground state vibrations identifies several modes that may be responsible for the charge evolution modulation. The 748 cm^{-1} and 796 cm^{-1} vibrational modes correspond to Ru-centered bpy twisting motion which gives rise to the out-of-plane rotation of the Ru-sided tpphz ligand. The 703 cm^{-1} vibrational mode corresponds to Cu-centered dmesp ligand motion (see Figure 3.6). The 846 cm^{-1} mode is especially interesting because it correlates the motion of Cu and Ru sites with the bridging tpphz ligand. The analysis presented here suggests that the electron and hole transfers can be modulated by ligand motions.

3.4 Conclusion

In this work, we have applied *ab initio* electron-nuclear dynamics to study the dynamical interplay between two metal-centered charge transfer states in a bimetallic complex. The photochemical dynamics were initiated by photoexcitation of the Ru-centered MLCT state. Electronic dynamics show that although there is a fast partial electron-hole recombination, the Ru-centered MLCT largely remains in its photoexcited state because the Ru-*d* reorganization prevents it from a complete coherent decay to the ground state. Electron-nuclear

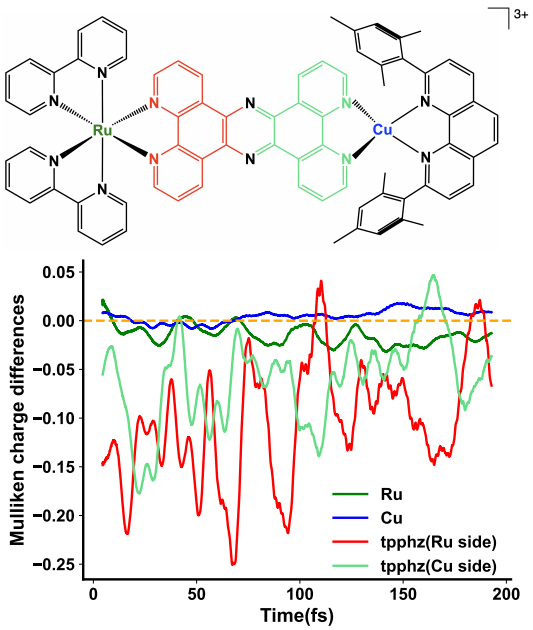

Figure 3.7: Evolution of Mulliken charge differences of selected fragments. The charge evolutions of Cu and Ru sides of the tpphz ligand are separately plotted.

Ehrenfest dynamics show that the molecular vibrations on the excited state lead to a small rotational motion of the tpphz bridge and closing motion of the mesityl ligands. These vibrational modes are seen to drive the metal-to-metal charge transfer event with both electron and hole populations being transferred in a concerted dynamics.

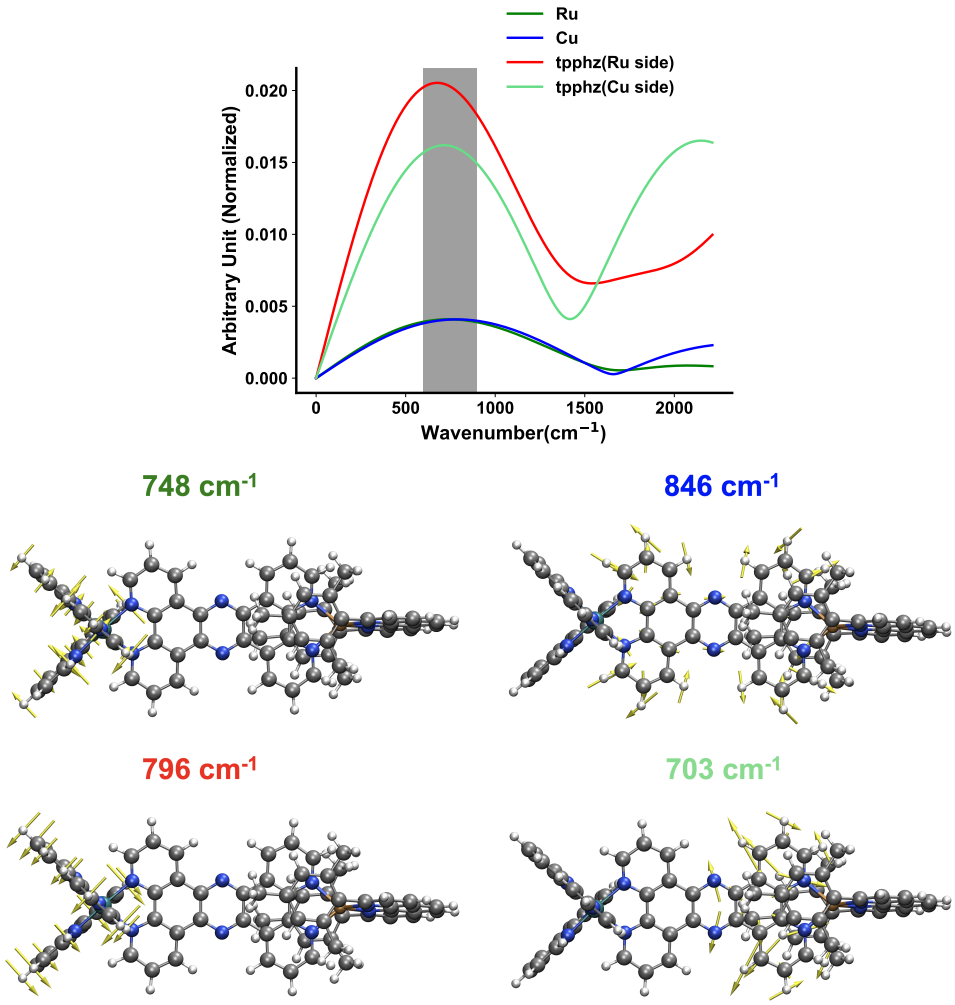

Figure 3.8: (**Top Panel**): Fourier transform (FT) of the time-evolution of Mulliken change difference. Areas between 600 and 900 cm^{-1} are shaded in grey. (**Bottom Panel**): Ground state vibrational modes in the range of 600-900 cm^{-1} with displacement vectors.

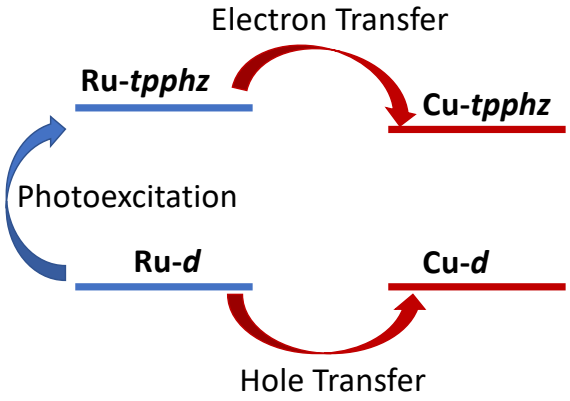

Figure 3.9: Proposed excited state metal-to-metal charge transfer mechanism.

Chapter 4

SITE-SPECIFIC ELECTRONIC STRUCTURE OF COVALENTLY LINKED BIMETALLIC DYADS FROM NITROGEN K-EDGE X-RAY ABSORPTION SPECTROSCOPY

When studying PET in bimetallic complexes, we are usually interested in how electron density changes with time. Experimentally, ultrafast spectroscopy is required to unravel the earliest time dynamics. However, it is difficult to use the common optical transient absorption spectroscopy because of overlapping absorbance of chromophore centers. Thus high spatial sensitivity is required. Unlike UV-vis spectroscopy, where the valence electrons are excited, in X-ray spectroscopy, core electrons are excited. X-ray absorption spectroscopy is element-specific due to large energy gaps of core electrons and is also sensitive to local environments. Depending on core levels, X-ray spectroscopy can be categorized into K-edge, L-edge, M-edge, etc. K-edge spectra originate from excitations out of 1s orbitals. N K-edge can be a good signature for change transfer in bimetallic complexes because N atoms appear in both the inner coordination shell of metal centers and the bridging ligand. Our goal is to study static N K-edge and to see if is it possible to do time-resolved N K-edge spectra in order to track excited state dynamics.

In this chapter, a nitrogen K-edge X-ray absorption near-edge structure (XANES) survey is presented for tetrapyrido[3,2-a:2′,3′-c:3″,2′-h:2‴,3‴-j]phenazine (tpphz)-bridged bimetallic assemblies that couple chromophore and catalyst transition metal complexes for light-driven catalysis, as well as their individual molecular constituents. We demonstrate the high N site sensitivity of the N pre-edge XANES features, which are energetically well-separated for the phenazine bridge N atoms and for the individual metal-bound N atoms of the inner coordination sphere ligands. By comparison with the time-dependent density functional

theory calculated spectra, we determine the origins of these distinguishable spectral features. We find that metal coordination generates large shifts toward higher energy for the metal-bound N atoms, with increasing shifts for $3d < 4d < 5d$ metal bonding. This is attributed to increasing ligand-to-metal σ donation that increases the effective charge of the bound N atoms and stabilizes the N 1s core electrons. In contrast, the phenazine bridge N pre-edge peak is found at a lower energy due to stabilization of the low energy electron accepting orbital localized on the phenazine motif. While no sensitivity to ground state electronic coupling between the individual molecular subunits was observed, the spectra are sensitive to structural distortions of the tpphz bridge. These results demonstrate N K-edge XANES as a local probe of electronic structure in large bridging ligand motifs, able to distinctly investigate the ligand-centered orbitals involved in metal-to-ligand and ligand-to-ligand electron transfer following light absorption. This chapter is adapted with permission from Elizabeth S. Ryland, Xiaolin Liu, Gaurav Kumar, Sumana L. Raj, Zhu-Lin Xie, Alexander K. Mengele, Sven S. Fauth, Kevin Siewerth, Benjamin Dietzek-Ivanšić, Sven Rau, Karen L. Mulfort, Xiaosong Li, and Amy A. Cordones. *J. Chem. Phys.* ***2024****, 160, 084307.*[3]

4.1 Introduction

Molecular donor/acceptor assemblies for solar energy capture and fuel production are often built of combined chromophore, bridge, and catalytic subunits designed to promote the unidirectional charge separation and multiple charge accumulation necessary for artificial photosynthesis.[102,120–126] The efficacy of these molecular assemblies as multi-electron multi-proton photocatalysts depends not only on the functionality of the individual parts but also on the intricate donor-acceptor interactions between the chromophore–bridge–catalytic subunits, as well as on how these interactions are modulated by the presence of electrons and protons on the complex.[127,128] Transition metals are readily incorporated into the design of such assemblies due to their tunable electronic structures and geometries, resulting in broad interest in assemblies of transition metal complex chromophores and catalysts, covalently linked using a conductive bridge, to facilitate efficient light-induced directional electron

transfer.[102,121,123–125]

Understanding the mechanistic roles of the molecular donor, acceptor, and bridging subunits in solar energy conversion necessitates understanding the electronic structure in both the ground state and reactive photo-excited states with high spatial sensitivity (localization to molecular moieties) as well as specificity to the donor and acceptor valence orbitals that participate in charge transfer. The mechanisms for charge transfer that underpin energy conversion processes for large, multinuclear molecular assemblies are often studied with optical spectroscopy methods.[1,76,77,94,96,129–134] While optical spectroscopy can be applied with high time resolution to capture the ultrafast dynamics of charge migration, optical spectra are not explicitly site-selective as the probed transitions are between delocalized valence orbitals. Furthermore, the interpretation of such measurements can be complicated by the overlapping optical features of the donor and acceptor moieties[1] or by the absence of visible wavelength spectral features for some commonly employed molecular catalysts.[4,129,135] Here, we instead pursue N K-edge X-ray absorption near-edge structure (XANES) spectroscopy as a probe of electronic structure for covalently bridged chromophore/catalyst assemblies, as conceptually illustrated in Figure 4.1. We demonstrate site-specific spectral features to separately probe the unoccupied ligand-centered orbitals of the chromophore, catalyst, and linking bridge moieties that directly participate in the light-driven electron transfer and charge accumulation in these systems.

XANES is an element-specific technique that probes transitions between atomic core levels and the unoccupied valence orbitals of a molecule. Metal L-edge and K-edge XANES spectroscopies (along with other metal edge X-ray spectroscopies) have been successfully employed to probe the excited state charge redistribution between two distinct metal sites in heterobimetallic donor-acceptor assemblies.[1,96,101,136,137] Here, we instead focus on the use of *ligand atom* K-edge XANES spectroscopy, which provides an additional tool to monitor charge localization beyond the metal coordination spheres and can resolve the intra-ligand charge transfer processes that underpin directional charge transfer across the assembly. Nitrogen K-edge spectroscopy is especially relevant to the field of molecular solar energy con-

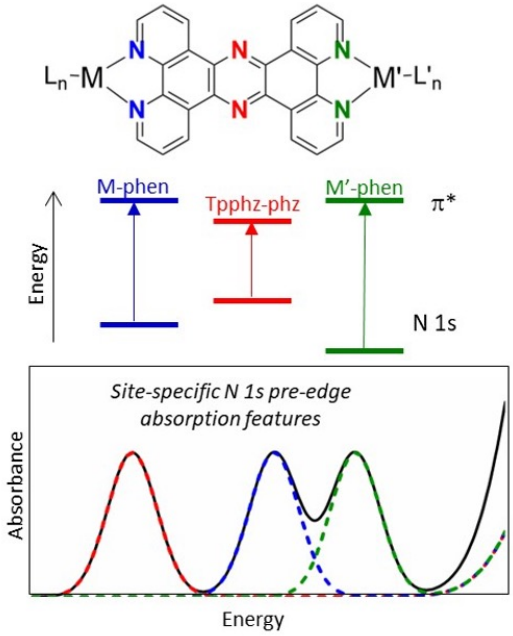

Figure 4.1: Schematic illustration of the tpphz-bridged M-M′ dyads investigated herein and the site-specific N K-edge absorption features that enable localized probing of the metal-bound and bridging ligand valence electronic structure. Pre-edge absorption features probing transitions of the N 1s electrons to the unoccupied valence orbitals can be resolved for each of the unique set of metal-bound phenanthroline (M-phen, blue and green) and tpphz-phenazine (tpphz-phz, red) N atoms within the dyad.

version due to the ubiquity of N-containing ligands in synthetically designed charge-transfer systems, both in metal coordinating ligands and in conductive linker molecules.[121,127] The N K-edge XANES spectra of aromatic heterocyclic ligands are characterized by a sharp and high-intensity pre-edge peak attributed to the transitions of N 1s core electrons to the lowest unoccupied π^* orbital of the ligand (illustrated schematically in Figure 4.1). This makes the N K-edge pre-edge feature a direct probe of the electron-accepting orbitals involved in metal-ligand or ligand–ligand charge transfer. N K-edge XANES has been successfully applied to investigate the electronic structure in the ground and/or excited states of electron-accepting ligand-based orbitals in metalloporphyrins and metal–polypyridyl complexes.[138–144] The energies and intensities of the N pre-edge absorption features of transition metal complexes have been assessed to reveal the metal-dependence of local charge on ligand N atoms,[138,139] changes in metal-ligand covalency,[141,145] and time-dependent changes in ligand electronic structures following optical excitation of charge transfer excited states.[140,142,146]

Herein, we extend N K-edge XANES to multi-valent systems with multiple distinct nitrogen sites contained in both metal-bound and bridging polypyridyl ligands. Specifically, we investigate donor/acceptor assemblies that contain the conductive bridging ligand tetrapyrido[3,2-a:2′,3′-c:3″,2′-h:2‴,3‴-j]phenazine (tpphz), which has been used extensively to link transition metal chromophore and catalytic complexes.[75–77,127] The tpphz bridge is characterized by a low-lying acceptor orbital localized on the central phenazine motif.[76,77,147] This serves to enable electron-hopping-type charge-transfer mechanisms in tpphz-bridged dyads, as well as to facilitate the accumulation of multiple electrons within the assembly. The presence of the extended π-system in tpphz has also been found to improve ligand stability against dissociation.[148] Given the centrally located N atoms of the tpphz bridge, we aim to identify if N K-edge XANES can provide a local probe of the electron-accepting orbitals on the bridge phenazine motif, distinct from the acceptor orbitals on the metal-bound ligands. We present a N K-edge XANES survey of the bimetallic tpphz-bridged assemblies, as shown in Figure 4.2 (labeled according to their metal centers as M-M′), as well as the monometallic molecular subunits that comprise the dyads (with and without bridge-mimicking phenazine-

containing ligands) and the corresponding unbound ligands. We observe distinct pre-edge absorption peaks that can be mapped to different N sites in the assemblies and identify the origins of their energetic separation by comparison with time-dependent density functional theory (TDDFT) spectral simulations. We find that N K-edge XANES not only is sensitive to metal-bound vs unbound N atoms in the dyads but also is a sensitive probe of the degree of ligand-to-metal σ-donation for metal-bound polypyridyl ligands and structural distortion of the tpphz bridge.

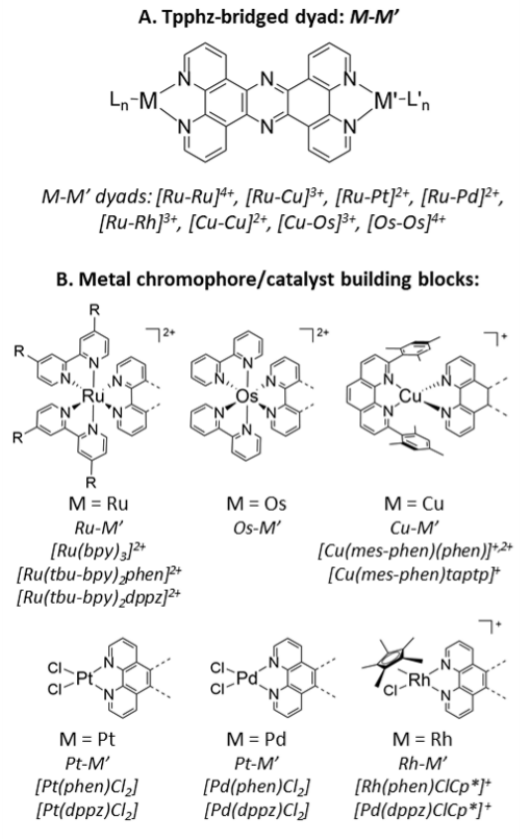

Figure 4.2: (a) Molecular structures of the tpphz-bridged bimetallic dyads, M-M′, investigated herein. (b) Molecular structures of the monometallic chromophore and catalyst complexes linked by tpphz in the dyads. Representative monometallic complexes, as listed below each structure, were also measured as references to aid in spectral interpretation. The full names and complete structures of each measured monometallic subunit, as well as of the measured unbound ligands, are listed in Supporting Information in Ref. 3

4.2 Methods

The molecular structures of all studied compounds, their name abbreviations, and synthesis details of the complexes can be found in Ref 3 and the supporting information therein.

4.2.1 N K-edge X-ray Absorption Spectroscopy

N K-edge XANES measurements were performed at two beamlines: beamline 7.3.1 at the Advanced Light Source (ALS) and beamline 8-2 at the Stanford Synchrotron Radiation Lightsource (SSRL). The solid samples were ground to a fine powder, applied to a carbon tape, and mounted on an Al sample stick. All data were recorded at room temperature in a vacuum chamber by scanning under incident X-ray energy and detecting the total electron yield (TEY) by measuring the drain current through the conductive sample mount. The spectra are normalized to the incident X-ray flux measured before taking the sample and represent an average of 3–9 measurements per sample. Both end stations employ spherical grating monochromators with an energy resolution of ∼0.2 eV. The scan-to-scan drift of the monochromator was corrected by applying an energy shift determined from simultaneous measurement of an in-line reference sample (SSRL data) or by measurement of a reference sample between each set of three scans (ALS data). Due to monochromator drift during data collection, we assign a ±0.05 eV confidence interval to the peak energies. Periods of larger drift were excluded from the data to avoid energy drift effects within a single scan (scan-to-scan shift of >0.1 eV excluded). Absolute energy calibration was achieved by setting the lowest energy peak of $[Ru(bpy)_3]^{2+}$ to 398.5 eV, which was determined against the internal reference NiF_2 using the second harmonic of the Ni L3-edge peak at 426.35 eV. The pre-edge peak energies were determined by fitting pseudo-Voigt distributions to the pre-edge peak region of 395–402 eV. The uncertainty from the peak-fitting is significantly smaller than the uncertainty of 0.05 eV due to monochromator instability.

4.2.2 DFT Calculations

All calculations were performed using the GAUSSIAN 16[149] package. We used the ωB97X-D functional[16] with the LANL2DZ effective core potential (ECP) and the corresponding basis set[87] on metal atoms and 6-31G(d) on non-metal atoms for geometry optimization and N K-edge simulations. The choice of the functional and basis set has been proven suitable for bimetallic systems in previous studies.[5,92,101] The optimized structures were confirmed as true minima by frequency calculations. Natural transition orbital (NTO)[110] and natural population[150] analyses were carried out to reveal the origin of excitations and peak energy differences, respectively. Energy-specific TD-DFT[151] was used to compute N K-edge spectra. All calculated spectra are shifted by 9.81 eV to match the experimental $[Ru(bpy)_3]^{2+}$ pre-edge peak energy. The N K-edge peak spacing is slightly overestimated in the simulations compared to the experiment, which is attributed in part to the intrinsic self-interaction errors of TD-DFT.[152]

4.3 Results and Discussion

4.3.1 Site Specificity of N K-edge XANES in Tpphz-bridged Bimetallic Assemblies

For multiple occurrences of N within a single tpphz-bridged donor/acceptor assembly, we observe that the unique sets of metal-bound N atoms and tpphz phenazine N atoms have distinct N K-edge XANES pre-edge features, as shown in Figure 4.3. This enables one to map the unoccupied ligand-based electronic structure with very high spatial specificity, separately probing the electron-accepting valence orbitals of the donor, bridge, and acceptor motifs involved in the excited state electron transfer.

Figure 4.3 (a) and (b) show the spectra of a tpphz-bridged $[Ru–Cu]^{3+}$ assembly, as recently synthesized by the Mulfort group and investigated for its excited state electron transfer processes.[1] $[Ru–Cu]^{3+}$ is selected as an illustrative due to the clear energetic spacing between the three pre-edge peaks of the three sets of unique N atoms: Cu-bound N, Ru-bound N, and bridge phenazine N atoms. The experimental (Figure 4.3 (a)) and calculated

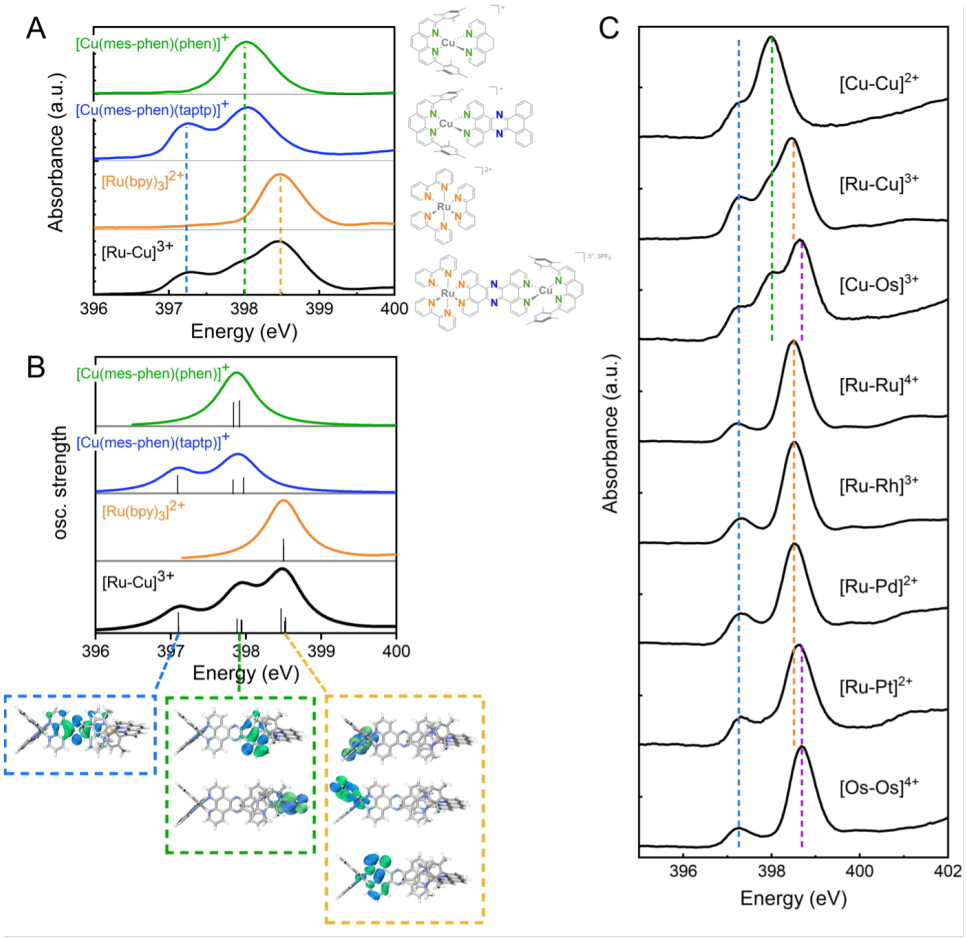

Figure 4.3: Experimental (a) and TDDFT calculated (b) N XANES spectra of donor–bridge–acceptor catalyst $[Ru–Cu]^{3+}$ (black) and its molecular constituents: $[Cu(mesphen)(phen)]^{+}$ (green) showing the peak attributed to Cu-bound N atoms, $[Cu(mesphen)(taptp)]^{+}$ (blue) showing the phenazine N peak in addition to the Cu-bound N peak, and $[Ru(bpy)_3]^{2+}$ (orange) showing the Ru-bound N peak. (c) Experimental N XANES spectra of other tpphz-bridged bimetallic dyads. The dashed lines indicate peak assignment: phenazine N (blue), Cu-bound N (green), 4d metal-bound N (orange), and 5d metal-bound N (purple).

(Figure 4.3 (b)) N K-edge XANES spectra of $[Ru–Cu]^{3+}$ (black trace) and its molecular building blocks (colored traces) are shown separately. The assignment of each pre-edge peak to a specific set of N atoms can be made directly by a comparison of the measured spectra of $[Ru–Cu]^{3+}$ with those of the individual molecular components. The highest energy pre-edge peak of $[Ru–Cu]^{3+}$ (Figure 4.3 (a), black) at 398.51 eV is due to the six near-degenerate Ru-bound N atoms, as evidenced by the comparison with the corresponding $[Ru(bpy)_3]^{2+}$ monomer (orange) and its single pre-edge peak at 398.53 eV. The middle $[Ru–Cu]^{3+}$ peak at 397.86 eV is due to the four Cu-bound N atoms, as can be seen from the alignment with the corresponding single pre-edge peak in the $[Cu(phen)(mes\text{-}phen)]^{+}$ monomer (green) at 398.05 eV. The lowest energy peak in the $[Ru–Cu]^{3+}$ spectrum at 397.26 eV is due to the two degenerate N atoms on the phenazine portion of the tpphz bridge. This is clear from the appearance of the low energy peak in $[Cu(phen)(taptp)]^{+}$ (blue) at 397.23 eV upon the addition of the phenazine-containing taptp ligand (relative to $[Cu(phen)(mes\text{-}phen)]^{+}$).

These mappings of the pre-edge peaks to distinct sets of N atoms are also confirmed by the TD-DFT calculations of N K-edge XANES spectra for the same $[Ru–Cu]^{3+}$ dyad and molecular subunits, which reproduce the measured spectra as shown in Figure 4.3(b). The transitions underlying the simulated spectra (sticks in Figure 4.3(b)) are investigated in more detail to identify the acceptor orbitals contributing to each absorption peak. This is illustrated by the natural transition orbitals (NTOs), which are generated from the acceptor orbitals involved in each of the electronic transitions and are shown below the $[Ru–Cu]^{3+}$ spectrum in Figure 4.3(b). From the NTO analysis, we determine that the phenazine N peak at 397.23 eV originates from transitions of the phenazine N 1s electrons to the lowest-lying unoccupied orbital of the molecular dyad, a π^* orbital localized across the three rings of the phenazine subunit of tpphz. The Cu-bound N peak at 398.05 eV is due to transitions of the Cu-bound N 1s electrons to an unoccupied π^* orbital delocalized across the phenanthroline portions of the mes-phen and tpphz ligands. We find that the calculated transitions corresponding to the mes-phen ligand cannot be resolved from those of the Cu-bound phenanthroline portion of tpphz. The Ru-bound N peak at 398.53 eV is due to the transitions of

the Ru-bound N 1s electrons to the unoccupied π^* orbitals of the bipyridine ligands and closest phenanthroline portion of tpphz. Again, we are unable to resolve separate absorption features distinguishing transitions of the Ru-bound bipyridine ligands vs the Ru-bound phenanthroline portion of tpphz. The findings of this NTO analysis are generally applicable across the full range of complexes. The measured spectra of the additional tpphz-bridged bimetallic dyads are shown in Figure 4.3(c).

The TD-DFT calculations were further used to investigate the source of the energetic splitting of the three peaks in the $[Ru–Cu]^{3+}$ spectrum by calculating the transition energy and the energy of the underlying N 1s and π^* acceptor orbitals. We find that the stabilization of the tpphz phenazine N peak relative to the metal-bound N peaks is primarily driven by a difference in the energies of their respective π^* acceptor orbitals. Consistent with previous work,[76,77]the lowest unoccupied orbital of the dyads is delocalized across the phenazine portion of the tpphz bridge, resulting in its lower energy pre-edge peak. This is generalizable across all dyads measured in this work (as shown in Fig. 3(c)). In contrast, we find that the transitions of the different metal-bonded N atoms appear at distinct energies primarily due to varying degrees of stabilization of the metal-bound N 1s orbitals. This trend of N 1s stabilization is generalizable across the range of 3d-to-5d metals measured herein but is metal-dependent, as discussed in the next section.

4.3.2 Metal-dependence of the Metal-bound N Peak Energy: Probe of Ligand-to-metal σ Donation

It is apparent from the dyad spectra shown in Figure 4.3(c) that the pre-edge peak energies corresponding to the metal-bound N atoms of the bimetallic dyads are highly metal-dependent and increase for $3d < 4d < 5d$ metal-bound N sites of the dyads. Here, we explore the underlying reason for this observed metal dependence. The trend is investigated more explicitly, as shown in Figure 4.4(a), which plots the fitted N XANES pre-edge peak energies for N atoms bonded directly to the metal center but only considers the monometallic subunits or homo-bimetallic dyads to avoid any challenges associated with fitting closely spaced

peaks in the hetero-bimetallic dyads. Both experimental (solid black circles) and simulated (open red circles) peak energies are shown. Additionally, the peak energy of the unbound mes-phen ligand is included to highlight the influence of metal binding more generally. The associated experimental and simulated spectra for representative homo-bimetallic complexes of 3d ($[Cu–Cu]^{2+}$), 4d ($[Ru–Ru]^{4+}$), and 5d ($[Os–Os]^{4+}$) metal systems are shown in Figure 4.4(b). In general, simulated spectra show excellent agreement with the experimental trends. The same general trend noted for the heterobimetallic dyads is shown in Fig. 4(a): metal coordination shifts the N pre-edge peak toward a higher energy and the extent of that shift increases as one goes from N atoms bound to $3d < 4d < 5d$ metals. Given the agreement between the calculated and experimental results, the TD-DFT calculated transitions are investigated in detail to understand the origin of the observed trend.

Generally, the TD-DFT calculations show that both core and unoccupied orbitals are significantly stabilized upon metal binding (and increasingly from 3d-to-5d metal binding) through a combination of long-range electrostatic and local chemical bonding effects. The electrostatic effect was isolated by simulating the spectra of the Ru-bound N atoms of $[Ru(bpy)_2(tpphz)]^{2+}$ in the presence of a point charge to mimic the introduction of a second positively charged metal ion, as shown in Figure 4.5. The presence of the point charge does not significantly change the calculated transition energy (compared to the magnitude of change shown in Figure 4.4) but results in significant stabilization of both the N 1s and ligand π^* orbitals. In contrast, we experimentally observe that metal binding to the ligand N atoms shifts the pre-edge peak toward higher energy, indicating that the N 1s stabilization is greater than the ligand π^* stabilization (Figure 4.4(c)). This difference from the purely electrostatic behavior is attributed to the local chemical bonding interactions between the ligand N and bonded metal.

Overall, we observe that this larger degree of stabilization of the N 1s orbital relative to the ligand π^* is responsible for the increasing transition energies of the unbound $< 3d < 4d < 5d$ metal-bonded ligands. This trend is consistent with the dominant σ-donating character of polypyridyl ligands,[153] such that the ligand-to-metal σ donation increases the effective charge

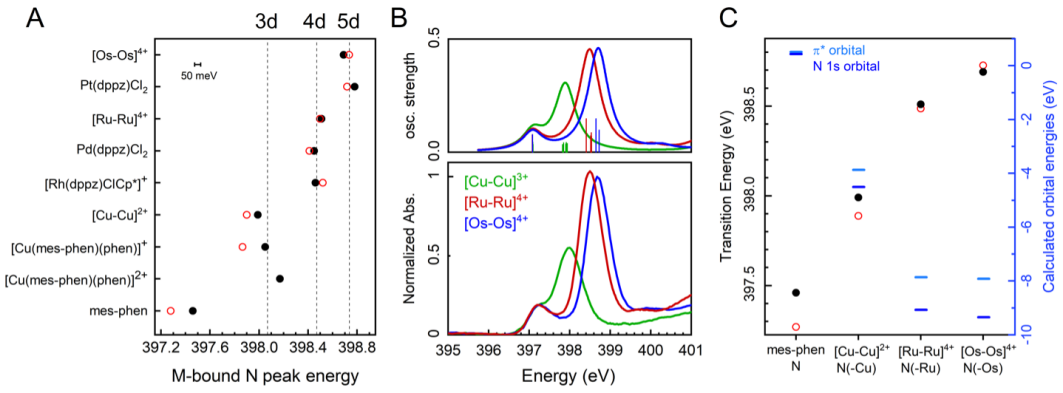

Figure 4.4: (a) Experimental (black circles) and TD-DFT calculated (red hollow circles) N pre-edge peak energies for a series of mono- and bimetallic molecules. The vertical lines highlight a comparison of 3d vs 4d vs 5d metal-bound N atoms, where the line indicates the average value of all data points for each metal type. (b) Computed (top) and experimental (bottom) N XAS spectra for [Cu–Cu]$^{2+}$, [Ru–Ru]$^{4+}$, and [Os–Os]$^{4+}$. Experimental spectra are normalized to the phenazine N bridge pre-edge peak at 397.2 eV, where all three complexes have an equivalent number of N atoms (N = 2). (c) Plot of the transition energy (left axis, experimental in black circles and calculated in open red circles) and underlying calculated relative orbital energies (right axis, N 1s in dark blue line and lowest unoccupied π^* orbital in cyan line). This plot illustrates that the increase in the N peak energy derives from a greater stabilization of the N 1s orbital (dark blue) relative to the electron-accepting π^* orbital (light blue). For clarity, the calculated N 1s orbital (dark blue) and π^* orbital (light blue) energies are plotted on a shared right axis such that the energies align for the mes-phen molecule.

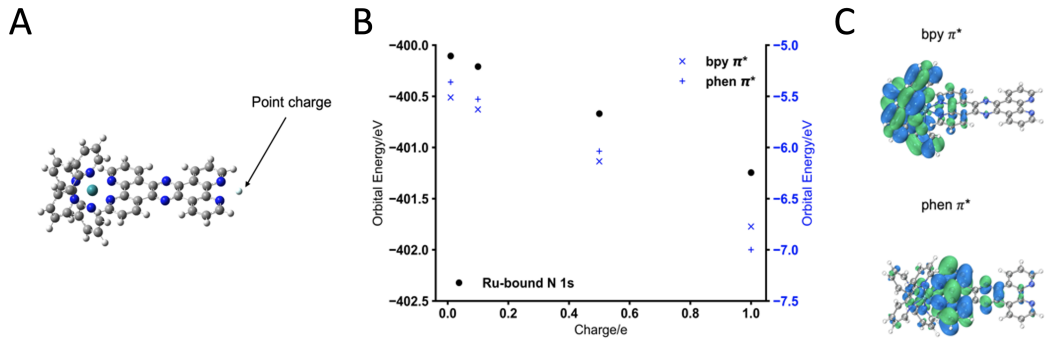

Figure 4.5: Electrostatic effect simulated by a point charge model. (a) A positive charge is placed at the Pt coordinate in a RuPt complex, with Pt moiety removed. (b) The Ru-bound N 1s orbital energies (left axis, black dot) and electron-accepting orbital energies (right axis, blue crosses) are calculated with varied point charge values. (c) The bpy and phen π^* electron-accepting orbitals.

of the ligand N atoms and stabilizes the N 1s core levels (due to decreased shielding in nuclear charge). As stronger metal-ligand interactions are expected for the more diffuse 5d and 4d metal orbitals,[154] increasing the σ donation with respect to the 3d metals is reflected by the increasing degree of N 1s stabilization (and the resulting increase in the pre-edge peak energies). The calculated natural charges of the metal-bound N atoms partially support the correlation between the effective charge of the N atoms and the measured and calculated transition energies, as shown in Figure 4.6. A large positive increase in N effective charge is predicted for the 4d and 5d bound N atoms relative to the Cu-bound N atoms; however, no systematic trend is predicted between the 4d vs 5d bound N atoms. Weaker contributions of metal-to-ligand π backdonation, which also increases for the 5d metals, could also affect the N pre-edge peak energies. However, we suggest that the resulting spectral shift would be minor as the destabilization of the π^* accepter orbital and reduction of the N atom effective charge (leading to destabilization of the N 1s core level) would have opposing effects on the N 1s-to-π^* transition energy. We note that neither trend is predicted by the TD-DFT results, as shown in Figure 4.4(c). The effect of π backdonation could be investigated by a rigorous comparison of the N K-edge for a single metal with a series of increasingly π-accepting

ligands.

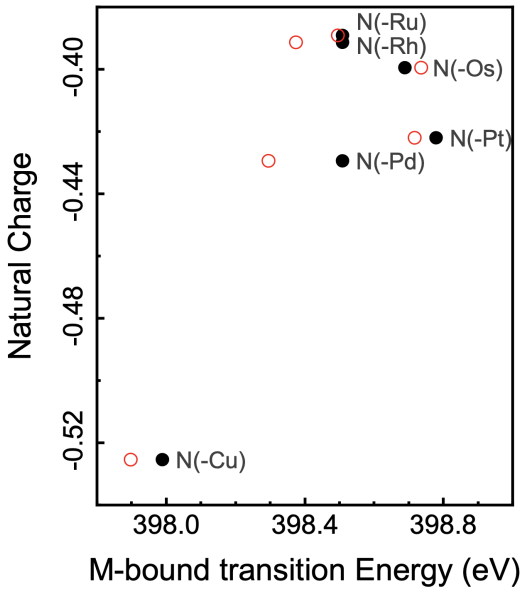

Figure 4.6: Natural Charge analysis computed from DFT calculation, plotted against measured (black circles) and calculated (hollow red circles) pre-edge peak energy for the M-bound N atoms.

Although the present study focuses on a limited subset of metal–polypyridyl complexes, many of the trends reported here are consistent with the previous reports of N K-edge XANES for similar classes of molecules. For example, the metalation of porphyrin, bipyridine, and phenanthroline ligands is known to shift the pre-edge peak toward a higher energy, consistent with the comparison of unbound and metal-bound ligands reported here.[139,143,145] While only complexes of a single 3d metal (Cu) were measured here, the previous work demonstrated a large spread of ∼0.5 eV in the N pre-edge peak energies of metalloporphyrins across the 3d periodic row.[138] The N pre-edge was found to increase (Mn < Fe < Co) and then decrease (Co > Ni > Cu > Zn), moving across the row and the transition energy correlated with N 1s stabilization and increasing the effective charge of the porphyrin N atoms, assigned on the basis of comparison with DFT calculations, and in agreement with the origins of the trends presented herein. We briefly explore the variation in the 3d metal-bound N

peak energies by varying the oxidation state of Cu in $[Cu(mes\text{-}phen)(phen)]^{n+}$ from Cu(I) to Cu(II) shown in Figure 4.4(a). As expected, Cu oxidation results in a shift toward a higher energy of the N pre-edge peak (by 0.13 eV) due to the increased ligand-to-metal σ donation (in this case, due to stabilization of the 3d orbitals) and resulting stabilization of the N 1s energy. We did not observe large variations or obvious trends within the few 4d or 5d metal complexes investigated here (d^6 to d^8). Instead, the largest variations observed in our survey are found as one moves down the period from 3d to 4d to 5d metals. The same trend was reported in the comparison of the N spectroscopy of Fe and Ru polypyridyl and porphyrin complexes,[138] and also appears to be generally observed in a large survey of metal–tris(bipyridine) complexes by Lukens et al.,[139,141] although not reported specifically. That the origin of the metal-dependent transition energies is attributed to N 1s stabilization here is further supported by a previous N K-edge X-ray photoelectron spectroscopy study, observing an increasing binding energy of the N 1s electron for Os > Ru > Fe $[M(bpy)_3]^{2+}$ complexes.

In summary, we find that the N K-edge XANES spectra have sufficient specificity to distinguish unique N sites in tpphz-bridged bimetallic dyads. The presence of the low-energy acceptor orbital on the tpphz phenazine motif results in the significant stabilization of the phenazine N pre-edge peak, making it a well-resolved probe of bridge electronic structures. In addition, the sensitivity of the metal-bound N pre-edge peak to the presence and strength of metal-ligand bonding interactions enables sufficient separation to specifically probe the 3d/4d/5d-bound ligands that participate in metal-ligand and ligand–bridge electron transfer. This specificity to unique N sites will now enable the evaluation of electronic couplings of the molecular constituents across a range of tpphz-bridged donor/acceptor assemblies. In the future, this spectroscopic distinction could additionally be used in the time domain to probe the intra-ligand excited state electron transfer processes that drive charge separation and the effects of multiple charge accumulation on the assemblies during catalysis.

4.3.3 Evaluation of Electronic Coupling between the Molecular Subunits of Tpphz-bridged Donor/acceptor Assemblies

With the above-mentioned assignments of the N K-edge XANES features, we now investigate how the combination of molecular subunits affects their intrinsic electronic structures. We check for electronic coupling between the unoccupied states of the phenazine and phenanthroline motifs by looking for changes in their respective pre-edge peaks when combined.

First, the effect of adding the conjugated phenazine moiety on the metal-bound phenanthroline ligands was evaluated. The metal-bound N pre-edge peak position was compared for monometallic complexes with either a phenanthroline (phen) or a dipyridophenazine (dppz) ligand, where dppz extends the phenanthroline ligand with a phenazine motif that emulates the central structure of the tpphz bridge. For a series of M-phen and M-dppz bound complexes with M = Cu, Ru, Rh, Pd, Pt, we find that addition of the phenazine bridge motif has a negligible effect (< 0.05 eV) on the energy of the metal-bound N pre-edge peak. Second, for a series of heterobimetallic Ru–M′ dyads ($[Ru–Ru]^{4+}$, $[Ru–Cu]^{3+}$, $[Ru–Pt]^{2+}$, $[Ru–Pd]^{2+}$, $[Ru–Rh]^{3+}$), we investigated the influence of the second metal (M′) linkage on the Ru-bound N preedge peak energies. Again, no significant effects (< 0.07 eV) were observed upon variation of the M′ acceptor motif or metal. The TD-DFT calculated N peak energies agree with the experimental results. From the lack of spectral changes observed, we infer that there is no significant ground state electronic coupling (above our $\sim$50 meV energy uncertainty) between the metal-bound ligands of the donor and acceptor sites or with the phenazine unit of the tpphz bridge. This is consistent with the previous conclusions drawn from optical and electrochemical characterization, finding that neither the metal-to-ligand charge transfer band in UV–Visible absorption nor the redox potentials of the Ru–polypyridyl chromophores are influenced by the addition of the acceptor moiety in $[Ru–Cu]^{3+}$,[1] $[Ru-Rh]^{3+}$,[135] $[Ru–Pt]^{2+}$,[155] $[Ru–Pd]^{2+}$,[156] or $[Ru–Os]^{4+}$.[75]

Surprisingly, we do observe a significant variation in the lower energy pre-edge peaks of the tpphz phenazine N atoms as a function of metal ligation and metal identity in the

tpphz-bridged M-M′ dyads, as shown in Figure 4.7. We find that any metal complexation to tpphz shifts the phenazine N pre-edge peak toward a lower energy compared to the unbound ligand, as observed in both measured and simulated spectra. Analysis of the orbital energies underlying the predicted transitions shows that the presence of metal ions has the same electrostatic effect described above for the metal-bound N peaks, stabilizing both the N 1s and lowest unoccupied valence orbitals. A slightly larger stabilization of the valence orbital relative to the 1s results in a small decrease in the transition energy. This decrease was also observed in the point-charge model (Figure 4.5), which found that the unoccupied valence orbitals were slightly more stabilized than the N 1s in the presence of a positive point charge.

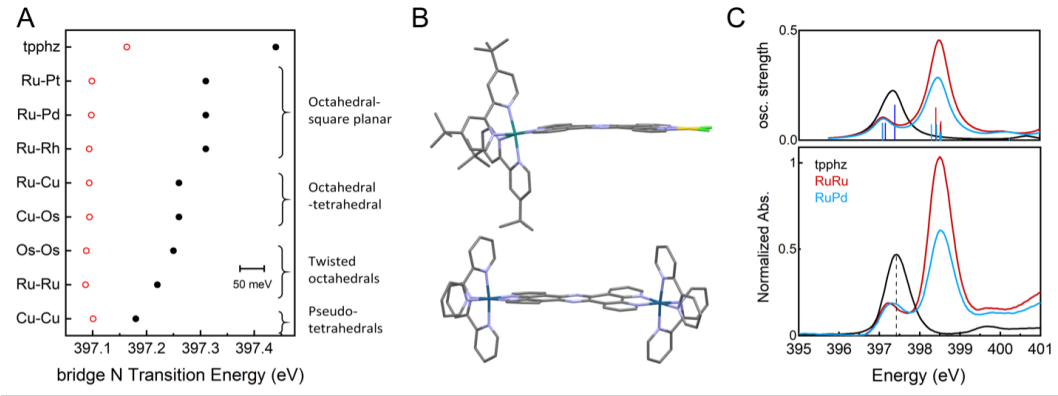

Figure 4.7: (a) Experimental (black circles) and calculated (red hollow circles) phenazine N pre-edge peak energies for the bridge phenazine nitrogen in M-tpphz-M′ dyads, grouped by molecular geometry. (b) Geometric crystal structures of $[Ru–Au]^{3+}$ (top)[4] and $[Os–Os]^{4+}$ (bottom),[5] showing flat vs twisted tpphz bridges. (c) Calculated (top) and experimental (bottom) N XANES spectra for $[Ru–Ru]^{4+}$, $[Ru–Pd]^{2+}$, and unmetallated tpphz. The experimental spectra are normalized to the phz bridge pre-peak at 397.2 eV, where both $[Ru–Ru]^{4+}$ and $[Ru–Pd]^{2+}$ have equivalent numbers of N atoms (N = 2).

Further variation in the phenazine N pre-edge peak position is observed as a function of the donor/acceptor metal complex identities. However, looking across the series of bimetallic complexes, there exists no obvious trend as a function of metal identity (3d vs 4d vs 5d). Furthermore, no similar metal-dependent trend is observed in the phenazine N peaks of the monometallic M-dppz bound complexes (variation < 0.08 eV). Thus, we consider that

this is not an electronic effect based on the specific metal attached but perhaps instead is a structural effect based on the coordination geometries of the two metals and the resulting intermolecular interactions in the solid state. Indeed, we find that the observed trend can be understood when the complexes are grouped by molecular geometries, as shown in Figure 4.7(a). We hypothesize two possible reasons for this structural effect as follows: (1) strain induced on the tpphz ligand or (2) π-stacking interactions between tpphz ligands.

First, in the crystalline forms of the dyads measured herein, distortions of the tpphz planarity depend on the geometry of the bound metal complexes. This was demonstrated by crystallography, finding waving or twisting distortions across tpphz for $[Ru–Ru]^{4+}$ and $[Os–Os]^{4+}$, respectively (as shown in Figure 4.7(b)), and a primarily bowing distortion across tpphz for $[Ru–Cu]^{3+}$ and $[Os–Cu]^{3+}$.[5] Although the crystal structures of the octahedral-square planar $[Ru–Rh]^{3+}$, $[Ru–Pd]^{2+}$, and $[Ru–Pt]^{2+}$ dyads have not been reported, the structure of an analogous $[Ru–Au]^{3+}$ dyad (as shown in Figure 4.7(b)) shows that the square planar motifs place little steric constraint on the bridge, resulting in minimal distortions from planarity.[4] The TD-DFT simulated spectra do not reproduce the experimental trend. However, this is not surprising as DFT was previously shown to underestimate the geometric distortion across the tpphz bridge as compared to the crystallographic geometries for these systems, as the distortions are largely induced by inter-molecular interactions in the crystal.[5] Therefore, it is possible that increasing tpphz structural distortion away from planarity decreases the energy of the bridge phenazine N pre-edge peak.

Second, intermolecular π interactions between tpphz ligands were demonstrated by X-ray crystallography for $[Ru(bpy)_2(tpphz)]^{2+}$, which formed π-stacked dimers.[157] While these dimers may be hindered for complexes containing bulky octahedral and tetrahedral ligand environments, they may occur more readily in the octahedral-square planar dyads. We suggest that it is also possible that π-stacking interactions between dyads increase the energy of the phenazine N pre-edge peak.

4.4 Conclusion

A nitrogen K-edge XANES survey of tpphz-bridged heterobimetallic assemblies that couple chromophore and catalyst transition metal complexes for light-driven catalysis, as well as their individual molecular constituents, is presented herein. We demonstrate a high specificity to the unique N sites in the N pre-edge XANES features, which are energetically well-separated for the tpphz bridge phenazine N atoms, and the donor and acceptor metal inner coordination sphere ligands. By comparison with the TD-DFT calculated spectra, we determine the origins of the differentiable spectral features observed. In a complement to the previous work probing N XANES in $3d^{5-10}$ coordination complexes,[138] we find that metal coordination generates large shifts toward higher energy for the metal-bound N atoms, with increasing shifts for $3d < 4d < 5d$ metal bonding. This is attributed to increasing ligand-to-metal σ donation that increases the effective charge of the bound N atoms and stabilizes the N 1s core electrons. In contrast, the tpphz phenazine N pre-edge peak is found at a lower energy due to its low energy electron-accepting orbital localized on the phenazine motif. While the spectra do not indicate any sensitivity to the electronic coupling between molecular components, they are sensitive to structural distortions of the tpphz bridge away from planarity.

The mapping of distinct N XANES peaks to bridges, donor ligands, or acceptor ligand N atoms enables one to separately probe the unoccupied electronic structure of the acceptor orbitals that participate in the metal-ligand and intra-ligand electron transfer processes that underpin the excited state charge separation in these photocatalytic assemblies. This report sets the stage for time-resolved N XANES experiments, which could potentially follow the redistribution of charge across chromophores, bridges, and catalyst ligands in real time. While several former studies demonstrated the use of time-resolved N K-edge XANES to track charge localization on the ligand following optical excitation of monometallic species,[140,142,146] our results here show that these efforts can be extended to heterobimetallic dyads, maintaining a high spatial specificity even in systems with multiple unique sets of N atoms. Future

work will make use of the well-separated pre-edge peaks of the donor, bridge, and acceptor motifs to monitor the dynamics and localization of charge across the tpphz ligand during the first steps of photocatalysis.

BIBLIOGRAPHY

[1] Hayes, D.; Kohler, L.; Hadt, R. G.; Zhang, X.; Liu, C.; Mulfort, K. L.; Chen, L. X. Excited State Electron and Energy Relays in Supramolecular Dinuclear Complexes Revealed by Ultrafast Optical and X-ray Transient Absorption Spectroscopy. *Chem. Sci.* **2018**, *9*, 860–875.

[2] Fairbanks, S. D.; Robertson, C. C.; Keene, F. R.; Thomas, J. A.; Williamson, M. P. Structural Investigation into the Threading Intercalation of a Chiral Dinuclear Ruthenium (II) Polypyridyl Complex through a B-DNA Oligonucleotide. *J. Am. Chem. Soc.* **2019**, *141*, 4644–4652.

[3] Ryland, E. S.; Liu, X.; Kumar, G.; Raj, S. L.; Xie, Z.-L.; Mengele, A. K.; Fauth, S. S.; Siewerth, K.; Dietzek-Ivanšić, B.; Rau, S. et al. Site-specific Electronic Structure of Covalently Linked Bimetallic Dyads from Nitrogen K-edge X-ray Absorption Spectroscopy. *J. Chem. Phys.* **2024**, *160*, 084307.

[4] Sorsche, D.; Schaub, M.; Heinemann, F. W.; Habermehl, J.; Kuhri, S.; Guldi, D.; Guthmuller, J.; Rau, S. π-Stacking Attraction vs. Electrostatic Repulsion: Competing Supramolecular Interactions in a Tpphz-bridged Ru (ii)/Au (iii) Complex. *Dalton Trans.* **2016**, *45*, 12846–12853.

[5] Xie, Z.-L.; Liu, X.; Valentine, A. J. S.; Lynch, V. M.; Tiede, D. M.; Li, X.; Mulfort, K. L. Bimetallic Copper/Ruthenium/Osmium Complexes: Observation of Conformational Differences Between the Solution Phase and Solid State by Atomic Pair Distribution Function Analysis. *Angew. Chem. Int. Ed.* **2022**, *61*, e202111764.

[6] Thomas, L. H. The Calculation of Atomic Fields. Math. Proc. Cambridge. 1927; pp 542–548.

[7] Fermi, E. Un Metodo Statistico per la Determinazione di Alcune Priorietà dell'Atomo. *Rend. Accad. Naz. Lincei.* **1927**, *6*, 32.

[8] Hohenberg, P.; Kohn, W. Inhomogeneous Electron Gas. *Physical review* **1964**, *136*, B864.

[9] Kohn, W.; Becke, A. D.; Parr, R. G. Density Functional Theory of Electronic Structure. *J. Phys. Chem.* **1996**, *100*, 12974–12980.

[10] Cramer, C. J. *Essentials of Computational Chemistry: Theories and Models*; John Wiley & Sons, 2013.

[11] Kohn, W.; Sham, L. J. Self-consistent Equations Including Exchange and Correlation Effects. *Physical review* **1965**, *140*, A1133.

[12] Becke, A. Density-functional Thermochemistry. III. The Role of Exact Exchange. *J. Chem. Phys.* **1993**, *98*, 5648–5652.

[13] Lee, C.; Yang, W.; Parr, R. G. Development of the Colle-Salvetti Correlation-energy Formula into a Functional of the Electron Density. *Phys. Rev. B* **1988**, *37*, 785.

[14] Vosko, S. H.; Wilk, L.; Nusair, M. Accurate Spin-dependent Electron Liquid Correlation Energies for Local Spin Density Calculations: a Critical Analysis. *Can. J. Phys.* **1980**, *58*, 1200–1211.

[15] Stephens, P. J.; Devlin, F. J.; Chabalowski, C. F.; Frisch, M. J. *Ab initio* Calculation of Vibrational Absorption and Circular Dichroism Spectra Using Density Functional Force Fields. *J. Phys. Chem.* **1994**, *98*, 11623–11627.

[16] Chai, J.-D.; Head-Gordon, M. Long-range Corrected Hybrid Density Functionals with Damped Atom–atom Dispersion Corrections. *Phys. Chem. Chem. Phys.* **2008**, *10*, 6615–6620.

[17] Runge, E.; Gross, E. K. Density-functional Theory for Time-dependent Systems. *Phys. Rev. Lett.* **1984**, *52*, 997.

[18] Gross, E. K.; Maitra, N. T. Introduction to TDDFT. *Fundamentals of Time-Dependent Density Functional Theory* **2012**, 53–99.

[19] Marques, M. A.; Gross, E. K. Time-dependent Density Functional Theory. *Annu. Rev. Phys. Chem.* **2004**, *55*, 427–455.

[20] Li, X.; Govind, N.; Isborn, C.; DePrince, A. E.; Lopata, K. Real-Time Time-Dependent Electronic Structure Theory. *Chem. Rev.* **2020**, *120*, 9951–9993.

[21] Goings, J. J.; Lestrange, P. J.; Li, X. Real-Time Time-Dependent Electronic Structure Theory. *WIREs Comput. Mol. Sci.* **2018**, *8*, e1341.

[22] Tully, J. C. Perspective: Nonadiabatic Dynamics Theory. *J. Chem. Phys.* **2012**, *137*, 22A301.

[23] Tully, J. C. Mixed Quantum-classical Dynamics. *Faraday Discuss.* **1998**, *110*, 407–419.

[24] González, L.; Lindh, R. *Quantum Chemistry and Dynamics of Excited States: Methods and Applications*; John Wiley & Sons, 2020.

[25] Drukker, K. Basics of Surface Hopping in Mixed Quantum/Classical Simulations. *J. Comput. Phys.* **1999**, *153*, 225–272.

[26] Li, X.; Tully, J. C.; Schlegel, H. B.; Frisch, M. J. Ab Initio Ehrenfest Dynamics. *J. Chem. Phys.* **2005**, *123*, 084106.

[27] Yam, V. W. *Photofunctional Transition Metal Complexes*; Springer, 2007; Vol. 123.

[28] Mabbs, F. E.; Machin, D. J. *Magnetism and transition metal complexes*; Courier Corporation, 2008.

[29] Gispert, J. R. *Coordination chemistry*; Wiley-VCH Weinheim, 2008; Vol. 483.

[30] Roundhill, D. M. *Photochemistry and photophysics of metal complexes*; Springer Science & Business Media, 2013.

[31] Lo, K. K.-W. *Inorganic and Organometallic Transition Metal Complexes with Biological Molecules and Living Cells*; Academic Press, 2016.

[32] Petkov, V. *Characterization of Materials*; John Wiley & Sons, Inc., 2012.

[33] Tiede, D. M.; Mardis, K. L.; Zuo, X. X-ray Scattering Combined with Coordinate-based Analyses for Applications in Natural and Artificial Photosynthesis. *Photosynth. Res.* **2009**, *102*, 267–279.

[34] Guinier, A. *X-ray Diffraction in Crystals, Imperfect Crystals, and Amorphous Bodies*; Courier Corporation, 1994.

[35] Feigin, L.; Svergun, D. I.; others *Structure Analysis by Small-angle X-ray and Neutron Scattering*; Springer, 1987; Vol. 1.

[36] Chu, B.; Hsiao, B. S. Small-angle X-ray Scattering of Polymers. *Chem. Rev.* **2001**, *101*, 1727–1762.

[37] Foster, M. D. X-ray Scattering Methods for the Study of Polymer Interfaces. *Crit. Rev. Anal. Chem.* **1993**, *24*, 179–241.

[38] Du, P.; Kokhan, O.; Chapman, K. W.; Chupas, P. J.; Tiede, D. M. Elucidating the Domain Structure of the Cobalt Oxide Water Splitting Catalyst by X-ray Pair Distribution Function Analysis. *J. Am. Chem. Soc.* **2012**, *134*, 11096–11099.

[39] Huang, J.; Blakemore, J. D.; Fazi, D.; Kokhan, O.; Schley, N. D.; Crabtree, R. H.; Brudvig, G. W.; Tiede, D. M. Domain Structure for an Amorphous Iridium-oxide Water-oxidation Catalyst Characterized by X-ray Pair Distribution Function Analysis. *Phys. Chem. Chem. Phys.* **2014**, *16*, 1814–1819.

[40] Batchellor, A. S.; Kwon, G.; Laskowski, F. A.; Tiede, D. M.; Boettcher, S. W. Domain Structures of Ni and NiFe (Oxy) Hydroxide Oxygen-evolution Catalysts from X-ray Pair Distribution Function Analysis. *J. Phys. Chem. C* **2017**, *121*, 25421–25429.

[41] Kwon, G.; Jang, H.; Lee, J.-S.; Mane, A.; Mandia, D. J.; Soltau, S. R.; Utschig, L. M.; Martinson, A. B.; Tiede, D. M.; Kim, H. et al. Resolution of Electronic and Structural Factors Underlying Oxygen-evolving Performance in Amorphous Cobalt Oxide Catalysts. *J. Am. Chem. Soc.* **2018**, *140*, 10710–10720.

[42] He, X.; Waldman, R. Z.; Mandia, D. J.; Jeon, N.; Zaluzec, N. J.; Borkiewicz, O. J.; Ruett, U.; Darling, S. B.; Martinson, A. B.; Tiede, D. M. Resolving the Atomic Structure of Sequential Infiltration Synthesis Derived Inorganic Clusters. *ACS Nano* **2020**, *14*, 14846–14860.

[43] Tiede, D. M.; Kwon, G.; He, X.; Mulfort, K. L.; Martinson, A. B. Characterizing Electronic and Atomic Structures for Amorphous and Molecular Metal Oxide Catalysts at Functional Interfaces by Combining Soft X-ray Spectroscopy and High-energy X-ray Scattering. *Nanoscale* **2020**, *12*, 13276–13296.

[44] Kwon, G.; Kokhan, O.; Han, A.; Chapman, K. W.; Chupas, P. J.; Du, P.; Tiede, D. M. Oxyanion Induced Variations in Domain Structure for Amorphous Cobalt Oxide Oxygen Evolving Catalysts, Resolved by X-ray Pair Distribution Function Analysis. *Acta Cryst. B* **2015**, *71*, 713–721.

[45] Zuo, X.; Tiede, D. M. Resolving Conflicting Crystallographic and NMR Models for Solution-state DNA with Solution X-ray Diffraction. *J. Am. Chem. Soc.* **2005**, *127*, 16–17.

[46] Zuo, X.; Cui, G.; Merz Jr, K. M.; Zhang, L.; Lewis, F. D.; Tiede, D. M. X-ray Diffraction "Fingerprinting" of DNA Structure in Solution for Quantitative Evaluation of Molecular Dynamics Simulation. *Proc. Natl. Acad. Sci. U.S.A.* **2006**, *103*, 3534–3539.

[47] Rambo, R. P.; Tainer, J. A. Bridging the Solution Divide: Comprehensive Structural Analyses of Dynamic RNA, DNA, and Protein Assemblies by Small-angle X-ray Scattering. *Curr. Opin. Struct. Biol.* **2010**, *20*, 128–137.

[48] Lipfert, J.; Doniach, S. Small-angle X-ray Scattering from RNA, Proteins, and Protein Complexes. *Annu. Rev. Biophys. Biomol. Struct.* **2007**, *36*, 307–327.

[49] Rybtchinski, B.; Sinks, L. E.; Wasielewski, M. R. Combining Light-harvesting and Charge Separation in a Self-assembled Artificial Photosynthetic System Based on Perylenediimide Chromophores. *J. Am. Chem. Soc.* **2004**, *126*, 12268–12269.

[50] Kelley, R. F.; Rybtchinski, B.; Stone, M. T.; Moore, J. S.; Wasielewski, M. R. Solution-phase Structure of an Artificial Foldamer: X-ray Scattering Study. *J. Am. Chem. Soc.* **2007**, *129*, 4114–4115.

[51] Bullock, J. E.; Carmieli, R.; Mickley, S. M.; Vura-Weis, J.; Wasielewski, M. R. Photoinitiated Charge Transport through π-stacked Electron Conduits in Supramolecular Ordered Assemblies of Donor-acceptor Triads. *J. Am. Chem. Soc.* **2009**, *131*, 11919–11929.

[52] Tiede, D. M.; Zhang, R.; Chen, L. X.; Yu, L.; Lindsey, J. S. Structural Characterization of Modular Supramolecular Architectures in Solution. *J. Am. Chem. Soc.* **2004**, *126*, 14054–14062.

[53] Megyes, T.; Jude, H.; Grósz, T.; Bakó, I.; Radnai, T.; Tárkányi, G.; Pálinkás, G.; Stang, P. J. X-ray Diffraction and DOSY NMR Characterization of Self-assembled Supramolecular Metallocyclic Species in Solution. *J. Am. Chem. Soc.* **2005**, *127*, 10731–10738.

[54] Deák, A.; Megyes, T.; Tárkányi, G.; Király, P.; Biczók, L.; Pálinkás, G.; Stang, P. J. Synthesis and Solution-and Solid-State Characterization of Gold (I) Rings with Short

Au...Au Interactions. Spontaneous Resolution of a Gold (I) Complex. *J. Am. Chem. Soc.* **2006**, *128*, 12668–12670.

[55] Lee, S. J.; Mulfort, K. L.; O'Donnell, J. L.; Zuo, X.; Goshe, A. J.; Wesson, P. J.; Nguyen, S. T.; Hupp, J. T.; Tiede, D. M. Supramolecular Porphyrinic Prisms: Coordinative Assembly and Solution Phase X-ray Structural Characterization. *Chem. Commun.* **2006**, 4581–4583.

[56] O'Donnell, J. L.; Zuo, X.; Goshe, A. J.; Sarkisov, L.; Snurr, R. Q.; Hupp, J. T.; Tiede, D. M. Solution-phase Structural Characterization of Supramolecular Assemblies by Molecular Diffraction. *J. Am. Chem. Soc.* **2007**, *129*, 1578–1585.

[57] Megyes, T.; Bálint, S.; Bakó, I.; Grósz, T.; Pálinkás, G. Complete Structural Characterization of Metallacyclic Complexes in Solution-phase Using Simultaneously X-ray Diffraction and Molecular Dynamics Simulation. *J. Am. Chem. Soc.* **2008**, *130*, 9206–9207.

[58] Lee, S. J.; Mulfort, K. L.; Zuo, X.; Goshe, A. J.; Wesson, P. J.; Nguyen, S. T.; Hupp, J. T.; Tiede, D. M. Coordinative Self-assembly and Solution-phase X-ray Structural Characterization of Cavity-tailored Porphyrin Boxes. *J. Am. Chem. Soc.* **2008**, *130*, 836–838.

[59] Holló-Sitkei, E.; Tárkányi, G.; Párkányi, L.; Megyes, T.; Besenyei, G. Steric Effects in the Self-Assembly of Palladium Complexes with Chelating Diamine Ligands. 2008.

[60] Mulfort, K. L.; Tiede, D. M. Supramolecular Cobaloxime Assemblies for H2 Photocatalysis: An Initial Solution State Structure-function Analysis. *J. Phys. Chem. B* **2010**, *114*, 14572–14581.

[61] Mulfort, K. L.; Mukherjee, A.; Kokhan, O.; Du, P.; Tiede, D. M. Structure-function Analyses of Solar Fuels Catalysts Using *in situ* X-ray Ccattering. *Chem. Soc. Rev.* **2013**, *42*, 2215–2227.

[62] Kim, I. S.; Borycz, J.; Platero-Prats, A. E.; Tussupbayev, S.; Wang, T. C.; Farha, O. K.; Hupp, J. T.; Gagliardi, L.; Chapman, K. W.; Cramer, C. J. et al. Targeted Single-site MOF Node Modification: Trivalent Metal Loading via Atomic Layer Deposition. *Chem. Mater.* **2015**, *27*, 4772–4778.

[63] Platero-Prats, A. E.; Li, Z.; Gallington, L. C.; Peters, A. W.; Hupp, J. T.; Farha, O. K.; Chapman, K. W. Addressing the Characterisation Challenge to Understand Catalysis in MOFs: the Case of Nanoscale Cu Supported in NU-1000. *Faraday Discuss.* **2017**, *201*, 337–350.

[64] Howe, J. D.; Morelock, C. R.; Jiao, Y.; Chapman, K. W.; Walton, K. S.; Sholl, D. S. Understanding Structure, Metal Distribution, and Water Adsorption in Mixed-metal MOF-74. *J. Phys. Chem. C* **2017**, *121*, 627–635.

[65] Jung, D.; Saleh, L. M.; Berkson, Z. J.; El-Kady, M. F.; Hwang, J. Y.; Mohamed, N.; Wixtrom, A. I.; Titarenko, E.; Shao, Y.; McCarthy, K. et al. A Molecular Cross-linking Approach for Hybrid Metal Oxides. *Nat. Mater.* **2018**, *17*, 341–348.

[66] Petkov, V.; Ren, Y.; Kabekkodu, S.; Murphy, D. Atomic Pair Distribution Functions Analysis of Disordered Low-Z Materials. *Phys. Chem. Chem. Phys.* **2013**, *15*, 8544–8554.

[67] Soderholm, L.; Skanthakumar, S.; Neuefeind, J. Determination of Actinide Speciation in Solution Using High-energy X-ray Scattering. *Anal. Bioanal. Chem.* **2005**, *383*, 48–55.

[68] Qiao, B.; Skanthakumar, S.; Soderholm, L. Comparative CHARMM and AMOEBA Simulations of Lanthanide Hydration Energetics and Experimental Aqueous-solution Structures. *J. Chem. Theory Comput.* **2018**, *14*, 1781–1790.

[69] Skanthakumar, S.; Jin, G. B.; Lin, J.; Vallet, V.; Soderholm, L. Linking Solution

Structures and Energetics: Thorium Nitrate Complexes. *J. Phys. Chem. B* **2017**, *121*, 8577–8584.

[70] Knope, K. E.; Skanthakumar, S.; Soderholm, L. Two Dihydroxo-bridged Plutonium (IV) Nitrate Dimers and Their Relevance to Trends in Tetravalent Ion Hydrolysis and Condensation. *Inorg. Chem.* **2015**, *54*, 10192–10196.

[71] Fujii, K.; Matsugami, M.; Ueno, K.; Ohara, K.; Sogawa, M.; Utsunomiya, T.; Morita, M. Long-Range Ion-Ordering in Salt-Concentrated Lithium-Ion Battery Electrolytes: A Combined High-Energy X-ray Total Scattering and Molecular Dynamics Simulation Study. *J. Phys. Chem. C* **2017**, *121*, 22720–22726.

[72] Zheng, J.; Tan, G.; Shan, P.; Liu, T.; Hu, J.; Feng, Y.; Yang, L.; Zhang, M.; Chen, Z.; Lin, Y. et al. Understanding Thermodynamic and Kinetic Contributions in Expanding the Stability Window of Aqueous Electrolytes. *Chem* **2018**, *4*, 2872–2882.

[73] Zobel, M.; Neder, R. B.; Kimber, S. A. Universal Solvent Restructuring Induced by Colloidal Nanoparticles. *Science* **2015**, *347*, 292–294.

[74] Zobel, M. Observing Structural Reorientations at Solvent-nanoparticle Interfaces by X-ray Diffraction - Putting Water in the Spotlight. *Acta Crystallogr. A* **2016**, *72*, 621–631.

[75] Bolger, J.; Gourdon, A.; Ishow, E.; Launay, J.-P. Mononuclear and Binuclear Tetrapyrido [3,2-a:2′,3′-c:3″,2′-h:2‴,3‴-j] phenazine (tpphz) Ruthenium and Osmium Complexes. *Inorg. Chem.* **1996**, *35*, 2937–2944.

[76] Chiorboli, C.; Rodgers, M. A.; Scandola, F. Ultrafast Processes in Bimetallic Dyads with Extended Aromatic Bridges. Energy and Electron Transfer Pathways in Tetrapyridophenazine-bridged Complexes. *J. Am. Chem. Soc.* **2003**, *125*, 483–491.

[77] Chiorboli, C.; Bignozzi, C. A.; Scandola, F.; Ishow, E.; Gourdon, A.; Launay, J. P. Photophysics of Dinuclear Ru(II) and Os(II) Complexes Based on the Tetrapyrido[3,2-a:2′,3′-c:3″,2′-h:2‴,3‴-j] phenazine (tpphz) Bridging Ligand. *Inorg. Chem.* **1999**, *38*, 2402–2410.

[78] Cunningham, C. T.; Cunningham, K. L.; Michalec, J. F.; McMillin, D. R. Cooperative Substituent Effects on the Excited States of Copper Phenanthrolines. *Inorg. Chem.* **1999**, *38*, 4388–4392.

[79] Ruthkosky, M.; Kelly, C. A.; Castellano, F. N.; Meyer, G. J. Electron and Energy Transfer from Cu^{I} MLCT Excited States. *Coord. Chem. Rev.* **1998**, *171*, 309–322.

[80] Blaskie, M. W.; McMillin, D. R. Photostudies of Copper (I) Systems. 6. Room-temperature Emission and Quenching Studies of Bis (2, 9-dimethyl-1, 10-phenanthroline) Copper (I). *Inorg. Chem.* **1980**, *19*, 3519–3522.

[81] Chen, L. X.; Jennings, G.; Liu, T.; Gosztola, D. J.; Hessler, J. P.; Scaltrito, D. V.; Meyer, G. J. Rapid Excited-state Structural Reorganization Captured by Pulsed X-rays. *J. Am. Chem. Soc.* **2002**, *124*, 10861–10867.

[82] Qiu, X.; Thompson, J. W.; Billinge, S. J. PDFgetX2: a GUI-driven Program to Obtain the Pair Distribution Function from X-ray Powder Diffraction Data. *J. Appl. Crystallogr.* **2004**, *37*, 678–678.

[83] Bergman, S. D.; Kol, M. π-Stacking Induced NMR Spectrum Splitting in Enantiomerically Enriched Ru (II) Complexes: Evaluation of Enantiomeric Excess. *Inorg. Chem.* **2005**, *44*, 1647–1654.

[84] Yang, L.; Powell, D. R.; Houser, R. P. Structural Variation in Copper (I) Complexes with Pyridylmethylamide Ligands: Structural Analysis with a New Four-coordinate Geometry Index, τ 4. *Dalton Trans.* **2007**, 955–964.

[85] Kohler, L.; Hayes, D.; Hong, J.; Carter, T. J.; Shelby, M. L.; Fransted, K. A.; Chen, L. X.; Mulfort, K. L. Synthesis, Structure, Ultrafast Kinetics, and Light-induced Dynamics of CuHETPHEN Chromophores. *Dalton Trans.* **2016**, *45*, 9871–9883.

[86] Kohler, L.; Hadt, R. G.; Hayes, D.; Chen, L. X.; Mulfort, K. L. Synthesis, Structure, and Excited State Kinetics of Heteroleptic Cu (I) Complexes with a New Sterically Demanding Phenanthroline Ligand. *Dalton Trans.* **2017**, *46*, 13088–13100.

[87] Hay, P. J.; Wadt, W. R. *Ab initio* Effective Core Potentials for Molecular Calculations. Potentials for the Transition Metal Atoms Sc to Hg. *J. Chem. Phys.* **1985**, *82*, 270–283.

[88] Miertuš, S.; Scrocco, E.; Tomasi, J. Electrostatic Interaction of a Solute with a Continuum. A Direct Utilizaion of AB Initio Molecular Potentials for the Prevision of Solvent Effects. *Chem. Phys.* **1981**, *55*, 117–129.

[89] Mara, M. W.; Fransted, K. A.; Chen, L. X. Interplays of Excited State Structures and Dynamics in Copper (I) Diimine Complexes: Implications and Perspectives. *Coord. Chem. Rev.* **2015**, *282*, 2–18.

[90] Canton, S. E.; Kjær, K. S.; Vankó, G.; Van Driel, T. B.; Adachi, S.-i.; Bordage, A.; Bressler, C.; Chabera, P.; Christensen, M.; Dohn, A. O. et al. Visualizing the Non-equilibrium Dynamics of Photoinduced Intramolecular Electron Transfer with Femtosecond X-ray Pulses. *Nat. Chem.* **2015**, *6*, 6359.

[91] Biasin, E.; Fox, Z. W.; Andersen, A.; Ledbetter, K.; Kjær, K. S.; Alonso-Mori, R.; Carlstad, J. M.; Chollet, M.; Gaynor, J. D.; Glownia, J. M. et al. Direct Observation of Coherent Femtosecond Solvent Reorganization Coupled to Intramolecular Electron Transfer. *Nat. Chem.* **2021**, *13*, 343–349.

[92] Liu, X.; Hayes, D.; Chen, L. X.; Li, X. Bridge-mediated Metal-to-metal Electron and Hole Transfer in a Supermolecular Dinuclear Complex: A Computational Study Using Quantum Electron-nuclear Dynamics. *J. Phys. Chem. A* **2023**, *127*, 1831–1838.

[93] Knapp, R.; Schott, A.; Rehahn, M. A Novel Synthetic Strategy toward Soluble, Well-defined Ruthenium (II) Coordination Polymers. *Macromolecules* **1996**, *29*, 478–480.

[94] Flamigni, L.; Encinas, S.; Barigelletti, F.; MacDonnell, F. M.; Kim, K.-J.; Puntoriero, F.; Campagna, S. Excited-state Interconversion between Emissive MLCT Levels in a Dinuclear Ru (II) Complex Containing a Bridging Ligand with an Extended π System. *Chem. Commun.* **2000**, *13*, 1185–1186.

[95] Torieda, H.; Nozaki, K.; Yoshimura, A.; Ohno, T. Low Quantum Yields of Relaxed Electron Transfer Products of Moderately Coupled Ruthenium(II)-cobalt(III) Compounds on the Subpicosecond Laser Excitation. *J. Phys. Chem. A* **2004**, *108*, 4819–4829.

[96] Canton, S. E.; Zhang, X.; Zhang, J.; van Driel, T. B.; Kjaer, K. S.; Haldrup, K.; Chabera, P.; Harlang, T.; Suarez-Alcantara, K.; Liu, Y. et al. Toward Highlighting the Ultrafast Electron Transfer Dynamics at the Optically Dark Sites of Photocatalysts. *J. Phys. Chem. Lett.* **2013**, *4*, 1972–1976.

[97] Schmittel, M.; Ganz, A. Stable Mixed Phenanthroline Copper (i) Complexes. Key Building Blocks for Supramolecular Coordination Chemistry. *Chem. Commun.* **1997**, 999–1000.

[98] Schmittel, M.; Lüning, U.; Meder, M.; Ganz, A.; Michel, C.; Herderich, M. Synthesis of Sterically Encumbered 2, 9-diaryl Substituted Phenanthrolines. Key Building Blocks for the Preparation of Mixed (bis-heteroleptic) Phenanthroline Copper (I) Complexes. *Heterocycl. Commun.* **1997**, *3*, 493–498.

[99] Sandroni, M.; Kayanuma, M.; Planchat, A.; Szuwarski, N.; Blart, E.; Pellegrin, Y.; Daniel, C.; Boujtita, M.; Odobel, F. First Application of the HETPHEN Concept to new Heteroleptic bis (diimine) copper (I) Complexes as Sensitizers in Dye Sensitized Solar Cells. *Dalton Trans.* **2013**, *42*, 10818–10827.

[100] Hayes, D.; Kohler, L.; Chen, L. X.; Mulfort, K. L. Ligand Mediation of Vectorial Charge Transfer in Cu (I) diimine Chromophore–Acceptor Dyads. *J. Phys. Chem. Lett.* **2018**, *9*, 2070–2076.

[101] Mara, M. W.; Phelan, B. T.; Xie, Z.-L.; Kim, T. W.; Hsu, D. J.; Liu, X.; Valentine, A. J. S.; Kim, P.; Li, X.; Adachi, S.-i. et al. Unveiling Ultrafast Dynamics in Bridged Bimetallic Complexes using Optical and X-ray Transient Absorption Spectroscopies. *Chem. Sci.* **2022**, *13*, 1715–1724.

[102] Wasielewski, M. R. Photoinduced Electron Transfer in Supramolecular Systems for Artificial Photosynthesis. *Chem. Rev.* **1992**, *92*, 435–461.

[103] Ponseca Jr, C. S.; Chábera, P.; Uhlig, J.; Persson, P.; Sundström, V. Ultrafast Electron Dynamics in Solar Energy Conversion. *Chem. Rev.* **2017**, *117*, 10940–11024.

[104] Cheng, Y.-C.; Fleming, G. R. Dynamics of Light Harvesting in Photosynthesis. *Annu. Rev. Phys. Chem.* **2009**, *60*, 241–262.

[105] Li, X.; Smith, S. M.; Markevitch, A. N.; Romanov, D. A.; Levis, R. J.; Schlegel, H. B. A Time-Dependent Hartree-Fock Approach for Studying the Electronic Optical Response of Molecules in Intense Fields. *Phys. Chem. Chem. Phys.* **2005**, *7*, 233–239.

[106] Isborn, C. M.; Li, X.; Tully, J. C. TDDFT Ehrenfest Dynamics: Collisions between Atomic Oxygen and Graphite Clusters. *J. Chem. Phys.* **2007**, *126*, 134307.

[107] Petrone, A.; Lingerfelt, D. B.; Rega, N.; Li, X. From Charge-Transfer to a Charge-Separated State: A Perspective from the Real-Time TDDFT Excitonic Dynamics. *Phys. Chem. Chem. Phys.* **2014**, *16*, 24457–24465.

[108] Ding, F.; Goings, J. J.; Liu, H.; Lingerfelt, D. B.; Li, X. Ab Initio Two-Component Ehrenfest Dynamics. *J. Chem. Phys.* **2015**, *143*, 114105.

[109] Donati, G.; Lingerfelt, D. B.; Petrone, A.; Rega, N.; Li, X. "Watching" Polaron Pair Formation from First-Principles Electron-Nuclear Dynamics. *J. Phys. Chem. A* **2016**, *120*, 7255–7261.

[110] Martin, R. L. Natural Transition Orbitals. *J. Chem. Phys.* **2003**, *118*, 4775–4777.

[111] Kasper, J. M.; Li, X. Natural Transition Orbitals for Complex Two-Component Excited State Calculations. *J. Comput. Chem.* **2020**, *41*, 1557–1563.

[112] Frisch, M. J.; Trucks, G. W.; Schlegel, H. B.; Scuseria, G. E.; Robb, M. A.; Cheeseman, J. R.; Scalmani, G.; Barone, V.; Petersson, G. A.; Nakatsuji, H. et al. Gaussian Development Version, Revision J.14+. Gaussian Inc. Wallingford CT 2020.

[113] Zhao, Y.; Truhlar, D. G. The M06 Suite of Density Functionals for Main Group Thermochemistry, Thermochemical Kinetics, Noncovalent Interactions, Excited States, and Transition Elements: Two New Functionals and Systematic Testing of Four M06-class Functionals and 12 Other Functionals. *Theor. Chem. Acc.* **2008**, *120*, 215–241.

[114] Grimme, S.; Antony, J.; Ehrlich, S.; Krieg, H. A Consistent and Accurate ab initio Parametrization of Density Functional Dispersion Correction (DFT-D) for the 94 Elements H-Pu. *J. Chem. Phys.* **2010**, *132*, 154104.

[115] Pritchard, B. P.; Altarawy, D.; Didier, B.; Gibson, T. D.; Windus, T. L. New Basis Set Exchange: An Open, Up-to-Date Resource for the Molecular Sciences Community. *J. Chem. Inf. Model.* **2019**, *59*, 4814–4820.

[116] Stevens, W. J.; Basch, H.; Krauss, M. Compact Effective Potentials and Efficient Shared-exponent Basis Sets for the First- and Second-row Atoms. *J. Chem. Phys.* **1984**, *81*, 6026–6033.

[117] Fraser, M. G.; van der Salm, H.; Cameron, S. A.; Blackman, A. G.; Gordon, K. C. Heteroleptic Cu(I) Bis-diimine Complexes of 6,6′-Dimesityl-2,2′-bipyridine: A Structural, Theoretical and Spectroscopic Study. *Inorg. Chem.* **2013**, *52*, 2980–2992.

[118] Mewes, S. A.; Dreuw, A. Density-based Descriptors and Exciton Analyses for Visualizing and Understanding the Electronic Structure of Excited States. *Phys. Chem. Chem. Phys.* **2019**, *21*, 2843–2856.

[119] Drummer, M. C.; Weerasooriya, R. B.; Gupta, N.; Askins, E. J.; Liu, X.; Valentine, A. J. S.; Li, X.; Glusac, K. D. Proton-Coupled Electron Transfer in a Ruthenium(II) Bipyrimidine Complex in Its Ground and Excited Electronic States. *J. Phys. Chem. A* **2022**, *126*, 4349–4358.

[120] Gust, D.; Moore, T. A.; Moore, A. L. Solar Fuels via Artificial Photosynthesis. *Acc. Chem. Res.* **2009**, *42*, 1890–1898.

[121] Ashford, D. L.; Gish, M. K.; Vannucci, A. K.; Brennaman, M. K.; Templeton, J. L.; Papanikolas, J. M.; Meyer, T. J. Molecular Chromophore–catalyst Assemblies for Solar Fuel Applications. *Chem. Rev.* **2015**, *115*, 13006–13049.

[122] Keijer, T.; Bouwens, T.; Hessels, J.; Reek, J. N. Supramolecular Strategies in Artificial Photosynthesis. *Chem. Sci.* **2021**, *12*, 50–70.

[123] Sun, L.; Hammarström, L.; Åkermark, B.; Styring, S. Towards Artificial Photosynthesis: Ruthenium–manganese Chemistry for Energy Production. *Chem. Soc. Rev.* **2001**, *30*, 36–49.

[124] Meyer, T. J. Chemical Approaches to Artificial Photosynthesis. *Acta Chem. Scand.* **1989**, *22*, 163–170.

[125] Magnuson, A.; Anderlund, M.; Johansson, O.; Lindblad, P.; Lomoth, R.; Polivka, T.; Ott, S.; Stensjö, K.; Styring, S.; Sundström, V. et al. Biomimetic and Microbial Approaches to Solar Fuel Generation. *Acc. Chem. Res.* **2009**, *42*, 1899–1909.

[126] Mulfort, K. L.; Utschig, L. M. Modular Homogeneous Chromophore–catalyst Assemblies. *Acc. Chem. Res.* **2016**, *49*, 835–843.

[127] Schulz, M.; Karnahl, M.; Schwalbe, M.; Vos, J. G. The Role of the Bridging Ligand in Photocatalytic Supramolecular Assemblies for the Reduction of Protons and Carbon Dioxide. *Coord. Chem. Rev.* **2012**, *256*, 1682–1705.

[128] Kranz, C.; Wächtler, M. Characterizing Photocatalysts for Water Splitting: from Atoms to Bulk and from Slow to Ultrafast Processes. *Chem. Soc. Rev.* **2021**, *50*, 1407–1437.

[129] Tschierlei, S.; Presselt, M.; Kuhnt, C.; Yartsev, A.; Pascher, T.; Sundström, V.; Karnahl, M.; Schwalbe, M.; Schäfer, B.; Rau, S. et al. Photophysics of an Intramolecular Hydrogen-Evolving Ru–Pd Photocatalyst. *Chem. Eur. J.* **2009**, *15*, 7678–7688.

[130] Tschierlei, S.; Karnahl, M.; Presselt, M.; Dietzek, B.; Guthmuller, J.; González, L.; Schmitt, M.; Rau, S.; Popp, J. Photochemical Fate: the First Step Determines Efficiency of H_2 Formation with a Supramolecular Photocatalyst. *Angew. Chem. Int. Ed.* **2010**, *49*, 3981–3984.

[131] Yang, C.; Zhou, Q.; Jiao, Z.; Zhao, H.; Huang, C.-H.; Zhu, B.-Z.; Su, H. Ultrafast Excited State Dynamics and Light-switching of $[Ru(phen)_2(dppz)]^{2+}$ in G-quadruplex DNA. *Commun. Chem.* **2021**, *4*, 68.

[132] Indelli, M. T.; Orlandi, M.; Chiorboli, C.; Ravaglia, M.; Scandola, F.; Lafolet, F.; Welter, S.; Cola, L. D. Electron Transfer Across Modular Oligo-*p*-phenylene Bridges in $Ru(bpy)_2(bpy–ph_n–DQ)^{4+}$(n= 1–5) Dyads. Unusual Effects of Bridge Elongation. *J. Phys. Chem. A* **2012**, *116*, 119–131.

[133] Staffilani, M.; Belser, P.; Hartl, F.; Kleverlaan, C. J.; De Cola, L. Photophysical Properties of Homometallic Ruthenium (II) and Osmium (II) Complexes with a bis(dipyridophenazine) Bridging Ligand. From Pico-to Microsecond Time Resolution. *J. Phys. Chem. A* **2002**, *106*, 9242–9250.

[134] Zedler, L.; Mengele, A. K.; Ziems, K. M.; Zhang, Y.; Wächtler, M.; Gräfe, S.; Pascher, T.; Rau, S.; Kupfer, S.; Dietzek, B. Unraveling the Light-activated Reaction Mechanism in a Catalytically Competent Key Intermediate of a Multifunctional Molecular Catalyst for Artificial Photosynthesis. *Angew. Chem. Int. Ed.* **2019**, *58*, 13140–13148.

[135] Mengele, A. K.; Kaufhold, S.; Streb, C.; Rau, S. Generation of a Stable Supramolecular Hydrogen Evolving Photocatalyst by Alteration of the Catalytic Center. *Dalton Trans.* **2016**, *45*, 6612–6618.

[136] Huijser, A.; Pan, Q.; Van Duinen, D.; Laursen, M. G.; El Nahhas, A.; Chabera, P.; Freitag, L.; González, L.; Kong, Q.; Zhang, X. et al. Shedding Light on the Nature of Photoinduced States Formed in a Hydrogen-generating Supramolecular RuPt Photocatalyst by Ultrafast Spectroscopy. *J. Phys. Chem. A* **2018**, *122*, 6396–6406.

[137] Liekhus-Schmaltz, C.; Fox, Z. W.; Andersen, A.; Kjaer, K. S.; Alonso-Mori, R.; Biasin, E.; Carlstad, J.; Chollet, M.; Gaynor, J. D.; Glownia, J. M. et al. Femtosecond X-ray Spectroscopy Directly Quantifies Transient Excited-state Mixed Valency. *J. Phys. Chem. Lett.* **2022**, *13*, 378–386.

[138] Garcia-Lastra, J. M.; Cook, P. L.; Himpsel, F.; Rubio, A. Communication: Systematic Shifts of the Lowest Unoccupied Molecular Orbital Peak in X-ray Absorption for a Series of 3d Metal Porphyrins. *J. Chem. Phys.* **2010**, *133*, 151103.

[139] Johnson, P. S.; Cook, P. L.; Zegkinoglou, I.; García-Lastra, J. M.; Rubio, A.; Ruther, R. E.; Hamers, R. J.; Himpsel, F. Electronic Structure of Fe-vs. Ru-based Dye Molecules. *J. Chem. Phys.* **2013**, *138*, 044709.

[140] Cordones, A. A.; Pemmaraju, C. D.; Lee, J. H.; Zegkinoglou, I.; Ragoussi, M.-E.; Himpsel, F. J.; de la Torre, G.; Schoenlein, R. W. Excited-State Charge Distribution

of a Donor- π–Acceptor Zn Porphyrin Probed by N K-Edge Transient Absorption Spectroscopy. *J. Phys. Chem. Lett.* **2021**, *12*, 1182–1188.

[141] Lukens, J. T.; DiMucci, I. M.; Kurogi, T.; Mindiola, D. J.; Lancaster, K. M. Scrutinizing Metal–ligand Covalency and Redox Non-innocence via Nitrogen K-edge X-ray Absorption Spectroscopy. *Chem. Sci.* **2019**, *10*, 5044–5055.

[142] Van Kuiken, B. E.; Cho, H.; Hong, K.; Khalil, M.; Schoenlein, R. W.; Kim, T. K.; Huse, N. Time-resolved X-ray Spectroscopy in the Water Window: Elucidating Transient Valence Charge Distributions in an Aqueous Fe (II) Complex. *J. Phys. Chem. Lett.* **2016**, *7*, 465–470.

[143] Zegkinoglou, I.; Ragoussi, M.-E.; Pemmaraju, C.; Johnson, P. S.; Pickup, D. F.; Ortega, J. E.; Prendergast, D.; De la Torre, G.; Himpsel, F. Spectroscopy of Donor-π–acceptor Porphyrins for Dye-sensitized Solar Cells. *J. Phys. Chem. C* **2013**, *117*, 13357–13364.

[144] Himpsel, F.; Cook, P. L.; de la Torre, G.; Garcia-Lastra, J.; Gonzalez-Moreno, R.; Guo, J.-H.; Hamers, R.; Kronawitter, C.; Johnson, P.; Ortega, J. et al. Design of Solar Cell Materials via Soft X-ray Spectroscopy. *J Electron Spectros Relat Phenomena* **2013**, *190*, 2–11.

[145] Büchner, R.; Fondell, M.; Haverkamp, R.; Pietzsch, A.; da Cruz, V. V.; Föhlisch, A. The Porphyrin Center as a Regulator for Metal–ligand Covalency and π Hybridization in the Entire Molecule. *Phys. Chem. Chem. Phys.* **2021**, *23*, 24765–24772.

[146] Jay, R. M.; Eckert, S.; Van Kuiken, B. E.; Ochmann, M.; Hantschmann, M.; Cordones, A. A.; Cho, H.; Hong, K.; Ma, R.; Lee, J. H. et al. Following Metal-to-ligand Charge-transfer Dynamics with Ligand and Spin Specificity Using Femtosecond Resonant Inelastic X-ray Scattering at the Nitrogen K-edge. *J. Phys. Chem. Lett.* **2021**, *12*, 6676–6683.

[147] Fees, J.; Kaim, W.; Moscherosch, M.; Matheis, W.; Klima, J.; Krejcik, M.; Zalis, S. Electronic Structure of the Molecular Light Switch $[Ru(bpy)_2(dppz)]^{2+}$ (dppz= dipyrido[3, 2-a: 2', 3'-c] phenazine). Cyclic Voltammetric, UV/Vis, and EPR/ENDOR Study of Multiply Reduced Complexes and Ligands. *Inorg. Chem.* **1993**, *32*, 166–174.

[148] Amthor, S.; Hernández-Castillo, D.; Maryasin, B.; Seeber, P.; Mengele, A. K.; Gräfe, S.; González, L.; Rau, S. Strong Ligand Stabilization Based on π-Extension in a Series of Ruthenium Terpyridine Water Oxidation Catalysts. *Chem. Eur. J.* **2021**, *27*, 16871–16878.

[149] Frisch, M. J.; Trucks, G. W.; Schlegel, H. B.; Scuseria, G. E.; Robb, M. A.; Cheeseman, J. R.; Scalmani, G.; Barone, V.; Petersson, G. A.; Nakatsuji, H. et al. Gaussian 16 Revision C.01. Gaussian Inc. Wallingford CT 2016.

[150] Reed, A. E.; Weinstock, R. B.; Weinhold, F. Natural Population Analysis. *J. Chem. Phys.* **1985**, *83*, 735–746.

[151] Liang, W.; Fischer, S. A.; Frisch, M. J.; Li, X. Energy-Specific Linear Response TDHF/TDDFT for Calculating High-Energy Excited States. *J. Chem. Theory Comput.* **2011**, *7*, 3540–3547.

[152] Lestrange, P. J.; Nguyen, P. D.; Li, X. Calibration of Energy-Specific TDDFT for Modeling K-Edge XAS Spectra of Light Elements. *J. Chem. Theory Comput.* **2015**, *11*, 2994–2999.

[153] Josephsen, J.; Schäffer, C. E. The Position of 2,2'-bipyridine and 1,10-phenanthroline in the Spectrochemical Series. *Acta Chem. Scand.* **1977**, *31a*, 813–824.

[154] McCusker, J. K. Electronic Structure in the Transition Metal Block and Its Implications for Light Harvesting. *Science* **2019**, *363*, 484–488.

[155] Habermehl, J.; Nauroozi, D.; Martynow, M.; Vilk, Y. E.; Beranek, R.; Guthmuller, J.; Rau, S. Synthesis and Hydrogen Evolving Catalysis of a Panchromatic Photochemical Molecular Device. *Sustainable Energy Fuels* **2020**, *4*, 619–624.

[156] Rau, S.; Schafer, B.; Gleich, D.; Anders, E.; Rudolph, M.; Friedrich, M.; Gorls, H.; Henry, W.; Vos, J. G. A Supramolecular Photocatalyst for the Production of Hydrogen and the Selective Hydrogenation of Tolane. *Angew. Chem. Int. Ed.* **2006**, *45*, 6215.

[157] Karnahl, M.; Kuhnt, C.; Ma, F.; Yartsev, A.; Schmitt, M.; Dietzek, B.; Rau, S.; Popp, J. Tuning of Photocatalytic Hydrogen Production and Photoinduced Intramolecular Electron Transfer Rates by Regioselective Bridging Ligand Substitution. *ChemPhysChem* **2011**, *12*, 2101–2109.